Published online 9 November 2022

Nucleic Acids Research, 2022, Vol. 50, No. 20 ***11755–11774***
https://doi.org/10.1093/nar/gkac1028

Selective degradation of tRNA^{Ser}(AGY) is the primary driver for mitochondrial seryl-tRNA synthetase-related disease

Tingting Yu[1,†], Yi Zhang[1,2,†], Wen-Qiang Zheng[2], Siqi Wu[3], Guoqiang Li[1], Yong Zhang[2], Niu Li[1], Ruen Yao[1], Pengfei Fang[3], Jian Wang[1,*] and Xiao-Long Zhou[2,*]

[1]Department of Medical Genetics and Molecular Diagnostic Laboratory, Shanghai Key Laboratory of Clinical Molecular Diagnostics for Pediatrics, Shanghai Children's Medical Center, School of Medicine, Shanghai Jiao Tong University, 1678 Dong Fang Road, Shanghai 200127, China, [2]State Key Laboratory of Molecular Biology, CAS Center for Excellence in Molecular Cell Science, Shanghai Institute of Biochemistry and Cell Biology, Chinese Academy of Sciences, University of Chinese Academy of Sciences, 320 Yue Yang Road, Shanghai 200031, China and [3]State Key Laboratory of Bioorganic and Natural Products Chemistry, Center for Excellence in Molecular Synthesis, Shanghai Institute of Organic Chemistry, University of Chinese Academy of Sciences, Chinese Academy of Sciences, 345 Lingling Road, Shanghai 200032, China

Received August 05, 2022; Revised October 13, 2022; Editorial Decision October 15, 2022; Accepted October 21, 2022

ABSTRACT

Mitochondrial translation is of high significance for cellular energy homeostasis. Aminoacyl-tRNA synthetases (aaRSs) are crucial translational components. Mitochondrial aaRS variants cause various human diseases. However, the pathogenesis of the vast majority of these diseases remains unknown. Here, we identified two novel *SARS2* (encoding mitochondrial seryl-tRNA synthetase) variants that cause a multisystem disorder. c.654–14T > A mutation induced mRNA mis-splicing, generating a peptide insertion in the active site; c.1519dupC swapped a critical tRNA-binding motif in the C-terminus due to stop codon readthrough. Both mutants exhibited severely diminished tRNA binding and aminoacylation capacities. A marked reduction in mitochondrial tRNA^{Ser}(AGY) was observed due to RNA degradation in patient-derived induced pluripotent stem cells (iPSCs), causing impaired translation and comprehensive mitochondrial function deficiencies. These impairments were efficiently rescued by wild-type *SARS2* overexpression. Either mutation caused early embryonic fatality in mice. Heterozygous mice displayed reduced muscle tissue-specific levels of tRNA^{Ser}s. Our findings elucidated the biochemical and cellular consequences of impaired translation mediated by SARS2, suggesting that reduced abundance of tRNA^{Ser}(AGY) is a key determinant for development of *SARS2*-related diseases.

GRAPHICAL ABSTRACT

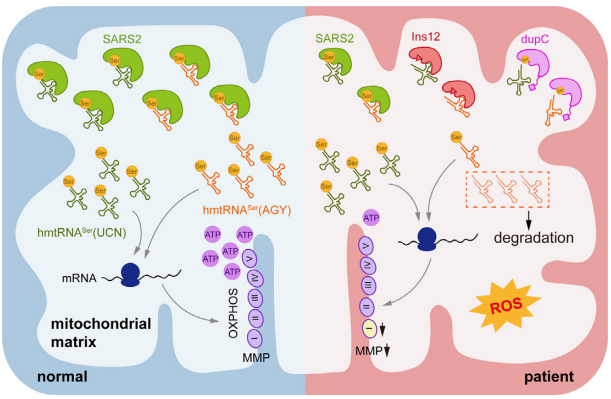

INTRODUCTION

Mitochondria provide ATP to cells via oxidative phosphorylation (OXPHOS). Mitochondria are dynamic organelles that undergo constant fusion and fission (1,2); they are also the main source of ROS (3). Several quality control mechanisms, including mitochondrial autophagy (mitophagy) (4,5), ensure functional mitochondria in cells.

Mitochondrial translation is pivotal for proper mitochondrial and cellular function by generating 13 essential subunits for respiratory chain complexes, while other

*To whom correspondence should be addressed. Tel: +86 21 5492 1247; Fax: +86 21 5492 1011; Email: xlzhou@sibcb.ac.cn
Correspondence may also be addressed to Jian Wang. Tel: +86 21 3808 7371; Email: labwangjian@shsmu.edu.cn
†The authors wish it to be known that, in their opinion, the first two authors should be regarded as Joint First Authors.

subunits are encoded by nuclear DNA (nDNA) (6–8). Aminoacyl-tRNA synthetases (aaRSs), divided into two classes (9), charge tRNAs with cognate amino acids to generate aminoacyl-tRNAs for mRNA translation (10). tRNA charging is performed via two reactions for most aaRSs: amino acid activation and aminoacylation (10,11).

Two sets of nDNA-encoded aaRSs are required to meet cytoplasmic and mitochondrial translation in human cells (12,13). Mutations in aaRS genes cause many tissue-specific human diseases, primarily affecting the central and peripheral nervous system, heart and muscle (12,14–17). The comprehensive effect of most mitochondrial aaRS (mito-aaRS) mutations on protein architecture, protein function, mitochondrial translation, and mitochondrial function remains poorly understood. Elucidation of etiology of individual aaRS disease–causing mutation is pivotal for patient diagnosis, treatment and prognosis.

SARS2 encodes class II mitochondrial seryl-tRNA synthetase (SerRS) (18), which aminoacylates two tRNAs, human mitochondrial $tRNA^{Ser}(AGY)$ ($hmtRNA^{Ser}(AGY)$) and $hmtRNA^{Ser}(UCN)$ (Figure 1A). $hmtRNA^{Ser}(AGY)$ is a highly unique tRNA in humans, lacking D-stem and D-loop structures; $hmtRNA^{Ser}(UCN)$ maintains canonical tRNA domains (6,18–20). Several mutations in *SARS2*, including c.1169A > G (p.D390G), c.667G > A (p.V223M), c.1031G > A (p.R344Q), c.1205G > A (p.R402H), c.1347G > A (causing mRNA mis-splicing), and c.1343A > T (p.H448L), have been associated with conditions such as HUPRA (hyperuricemia, pulmonary hypertension, renal failure, and alkalosis) syndrome (OMIM #613845) or progressive spastic paresis (21–26). These studies reinforce that *SARS2* is highly associated with human diseases; however, detailed information regarding pathogenesis of *SARS2*-related diseases remains elusive.

In this study, we examined a Chinese family with multisystem *SARS2*-related disorders, with both overlapping and distinct phenotypes of HUPRA syndrome and spastic paresis, and investigated the biochemical and cellular pathogenesis. Selective degradation of $hmtRNA^{Ser}(AGY)$ stood out as a primary and key determinant in inducing profound cellular deficiencies. We suggest that $hmtRNA^{Ser}(AGY)$ is particularly susceptible to RNA degradation if uncharged or unprotected by SARS2, likely because of its unstable structure. Our data provide a valuable basis for the onset, development, and diagnosis of *SARS2*-related diseases.

MATERIALS AND METHODS

Whole exome sequencing (WES) and variant verification

Genomic DNA was extracted from peripheral blood leukocytes using a Gentra Puregene Blood Kit (Qiagen, Hilden, Germany). DNA samples (3 μg of patient DNA) were subjected to WES using a SureSelect XT Human All Exon V6 reagent kit (Agilent Technologies, Santa Clara, CA, USA). The original sequencing data were assessed using FastQC (version0.11.2) for quality control. Sequence reads were aligned to the reference human genome (GRCh37/hg19) using NextGENe (SoftGenetics, StateCollege, PA, USA). All single-nucleotide variants and indels were saved in VCF format and uploaded to the Translational Genomics Expert platform (Flash Interpretation Biological Technology Company, Shanghai, China) for annotation, analysis, and prioritization (27). Variations in *SARS2* detected by WES were further verified in the pedigree by PCR amplification and Sanger sequencing.

Generation and identification of induced pluripotent stem cells (iPSCs)

Nucleofection and generation of iPSCs were performed with peripheral blood mononuclear cells (PBMCs) as previously described (28). Briefly, pEV SFFV-OCT4-E2A-SOX2 (OS), pEV SFFV-MYC-E2A-KLF4 (MK) and pEV SFFV-BCL-XL (Bcl-XL) episomal vectors were mixed and transferred to the cell pellet (1×10^6 cells). After nucleofection, the cells were transferred to a culture plate preseeded with feeder cells. The cells were cultured in reprogramming medium composed of knockout DMEM/F12 medium (Invitrogen, Carlsbad, CA, USA) supplemented with 10% KnockOut™ Serum Replacement (Invitrogen), 1% L-glutamine (Invitrogen), 2 mM nonessential amino acids (Invitrogen), 1% penicillin/streptomycin (Invitrogen), 1% 2-mercaptoethanol (Invitrogen), and 20 ng/ml FGF2 (PeproTech, Cranbury, NJ, USA) for 7 days. The cells were then cultured in PSCeasy medium (Cellapy, Beijing, China) until iPSCs were generated. The iPSCs were characterized by karyotyping, analysis of the expression of embryonic stem cell markers, teratoma formation, and *SARS2* sequencing.

Cell culture

PBMCs collected by Ficoll-Paque density gradient centrifugation were expanded for 6–10 days in serum-free erythroid culture medium (ECM) as described previously (28). Human iPSCs were cultured on Matrigel-coated plates (BD Biosciences, San Diego, CA, USA) in PSCeasy medium (Cellapy), which was changed daily. The iPSCs were passaged with EDTA (5×10^{-4} M) when reaching 60% confluence. Human embryonic kidney 239T (HEK293T) cells were obtained from the American Type Culture Collection (Manassas, VA, USA) and maintained in Dulbecco's modified Eagle's medium (DMEM) supplemented with 10% (v/v) fetal bovine serum (FBS) in a humidified atmosphere of 5% CO_2 atmosphere at 37°C.

Mitochondrial respiratory complex (MRC) activity

Mitochondria were isolated from iPSCs as previously described (29). A Bradford Protein Assay Kit (Beyotime, Shanghai, China) was used to quantify the mitochondrial samples. The activity of the MRC complexes was assessed by colorimetry using commercial kits (Abbkine, Wuhan, China) with a SynergyNEO Multi-Mode Reader (BioTek, Winooski, VT, USA) following manufacturer instructions.

Pulse-chase experiments

Pulse-chase experiments were conducted as previously described (30). For pulse labeling, iPSCs were pre-incubated

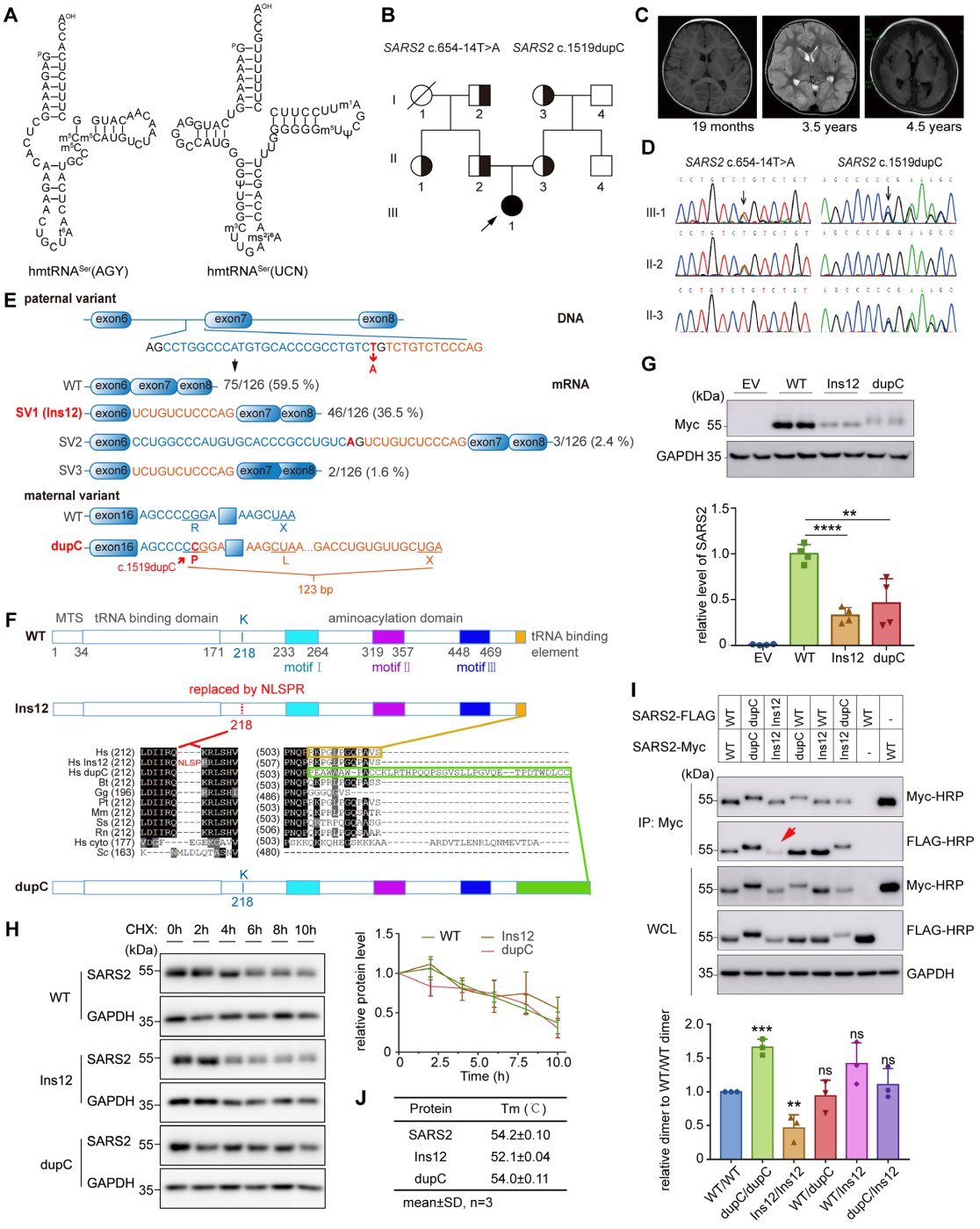

Figure 1. Two *SARS2* mutations identified in a Chinese pedigree with a multisystem disorder. (**A**) Secondary structures of human mitochondrial tRNA^{Ser}s. (**B**) Pedigree of the Chinese family. Half-solid symbols represent individuals carrying heterozygous *SARS2* mutations. Solid symbols represent the affected individual. The slash-through symbol represents a deceased individual. The proband is indicated by the arrow. (**C**) Cerebral MRI results of the patient showing normal findings at 19 months, diffuse edema at 3.5 years, and atrophy at 4.5 years of age. (**D**) DNA sequence identifying c.654–14T > A and c.1519dupC mutations in *SARS2*. (**E**) Scheme showing the impact of the c.654–14T > A and c.1519dupC mutations on *SARS2* transcription. (**F**) Primary sequence alignment showing the impact of c.654–14T > A and c.1519dupC mutations on the SARS2 amino acid sequence. Hs cyto, human SARS1; Sc, *Saccharomyces cerevisiae* cytoplasmic ThrRS; other sequences represent SARS2 from various species (Hs, *Homo sapiens*; Bt, *Bos taurus*; Gg, *Gallus gallus*; Pt, *Pan troglodytes*; Mm, *Mus musculus*; Ss, *Sus scrofa*; Rn, *Rattus norvegicus*). (**G**) Ectopic expression of wild-type and mutant SARS2 in HEK293T cells. The band intensities were measured and normalized to those of GAPDH (lower panel). (**H**) HEK293T cells were treated with CHX at the indicated time points. Western blot was performed on cell extracts using anti-Myc and anti-GAPDH antibodies. The band intensity was measured, normalized to GAPDH, and plotted as a percentage of the initial band intensity (right panel). (**I**) Detection of dimerization of wild-type and mutant SARS2 by Co-IP analysis. The red arrow indicates decreased homodimerization of Ins12-FLAG/Ins12-Myc. The coprecipitated FLAG-tagged proteins were measured and normalized to enriched Myc-tagged proteins (WT/WT dimer was defined as 1). (**J**) Tm values of purified mature SARS2 and mutants determined by TSA. Results in (G), (H) and (I) represent mean ± SD ($n = 3$–4), and P values were determined by unpaired two-tailed t-tests. $^{**}P < 0.01$, $^{***}P < 0.001$, $^{****}P < 0.0001$, ns: not significant.

in methionine- and cysteine-free medium and treated with 100 μg/mL emetine to block nDNA translation. The iPSCs were then incubated in 200 μCi/ml PRO-MIX ([^{35}S]-methionine and [^{35}S]-cysteine, PerkinElmer, Waltham, MA, US) to label the mitochondrial translation products. For chase labeling, 40 μg/ml chloramphenicol was added to the cell culture in advance. The labeling was carried out as described in the pulse labeling section, except that 100 μg/ml cycloheximide (CHX) was substituted for emetine. After labeling for 2 h, iPSCs were cultured in PSCeasy medium for 18 h (Chase). Protein samples were separated on 12–20% gradient SDS-polyacrylamide gels. Radioactive signals were detected by phosphor screens using the FLA-9000 fluorescent and radioisotope science imaging systems (Fijifilm, Tokyo, Japan) and quantified using ImageQuant v5.0 software (GE Healthcare, Chicago, IL, USA).

In vitro transcription of hmtRNA^{Ser}(AGY) and hmtRNA^{Ser}(UCN)

The T7 promoter sequence and the hmtRNA^{Ser}(AGY) and hmtRNA^{Ser}(UCN) genes were directly synthesized and cloned into the pTrc99b vector. The pTrc99b recombinant vector was used to amplify transcription template by PCR. tRNAs were transcribed as described previously (31). The obtained hmtRNA^{Ser} (AGY) and hmtRNA^{Ser} (UCN) were incubated at 85°C for 10 min, and then naturally cooled to room temperature. Biotin-labelled tRNAs were obtained as described previously (32).

Gene expression and protein purification

A construct expressing the full-length mature form of SARS2 with a C-terminal His$_6$-tag was developed according to a previous report (33). Constructs expressing Ins12 and dupC were generated using mutagenesis kits (TOYOBO, Osaka, Japan). *Escherichia coli* BL21-Codon Plus (DE3)-RIL cells were transfected with plasmids encoding wild-type and mutant human SARS2. A single clone was selected and cultured in Luria Broth at 37°C. When the cells reached the mid-log phase (OD value 0.6–0.8), isopropyl β-D-thiogalactoside was added at a final concentration of 100 μM to induce expression at 18°C for ∼16 h. Cells were collected by centrifugation at 5000 rpm and 4°C. Protein purification was performed as described previously (34). For crystallization purpose, the coding sequence of N-terminal Met^1-Val^{180}-truncated SARS2 (WT or Ins12) was inserted in a pET28a vector which expressed a His$_6$-tag at the N-terminal end of the SARS2 protein. The truncated proteins were initially purified using NTA affinity chromatography (Qiagen) and then further purified with an ion-exchange column (Cytiva, Uppsala, Sweden), followed by gel filtration using a Superdex 200 column (GE Healthcare) equilibrated with 20 mM Tris·HCl (pH 8.0), 150 mM NaCl, and 5 mM 2-mercaptoethanol. The peak fractions were concentrated for crystallization. All purification steps were performed at 4°C.

Structure determination

Crystal diffraction data were obtained from the National Facility for Protein Science in Shanghai at the Shanghai Synchrotron Radiation Facility. The dataset was processed using the HKL2000 program (35). The structures were determined by molecular replacement using Molrep (36). The bovine SARS2 structure (PDB No. 1WLE) was used as the search model. Iterative model building and refinement were performed using Coot (37) and Phenix (38). The data collection and refinement statistics were presented in Supplementary Table S2.

Study approval

The study was approved by the ethics committee of the Shanghai Children's Medical Center (Shanghai, China). Informed consent was obtained from the parents of the child included in this study. All procedures involving animals were reviewed and approved by the Institutional Animal Care and Use Committee of Shanghai Children's Medical Center.

Further information about the methodology is included in Supplemental Information.

RESULTS

Clinical presentation

The patient was a female aged 8.5 years, born to a nonconsanguineous Chinese couple (Figure 1B). A series of clinical phenotypes began to emerge in her first year of life, including brain atrophy observed by cerebral magnetic resonance imaging (MRI) at 4.5 years of age (Figure 1C). Detailed clinical manifestations were presented in the '*Clinical manifestation*' subsection of the Supplemental Information.

Compound heterozygous *SARS2* mutations were identified

To identify the causal gene, we performed WES and identified sixteen candidate single nucleotide variants in 14 genes (Supplementary Table S1). Among these, *SARS2* was recognized as the most likely causal gene because of its functional and clinical relevance. Two heterozygous variants of *SARS2*, (NM_017827.4) c.654–14T > A and c.1519dupC (p.R507Pfs*41), were detected in the patient. Sanger sequencing of family members revealed that c.654–14T > A and c.1519dupC were paternally and maternally inherited, respectively (Figure 1B, D). The *SARS2* variants (c.654–14T > A and c.1519dupC) had not been previously reported in public databases, such as the Human Genome Mutation Database (http://www.hgmd.cf.ac.uk), ClinVar (https://www.ncbi.nlm.nih.gov/clinvar), or the Genome Aggregation Database (gnomAD, http://gnomad-sg.org/), and were also absent from our local database (for individuals of the same ethnicity).

The two mutations caused mRNA mis-splicing and frameshifting

The c.654–14T > A variant was located at the 3′ end of intron 6 (Figure 1E). This paternal variant may potentially cause mRNA mis-splicing due to the presence of a 3′ splice site, AG, after mutation. Analyses of cDNA from peripheral leukocytes showed that wild-type mRNA accounted for approximately 60% of paternal RNA (Figure 1E). Considering the wild-type *SARS2* allele in paternal cells, it suggested

that the allele with the c.654–14T > A mutation still generated ∼10% normal transcripts. In addition, 36.5% mRNA (SV1) contained a 12-bp intron retention, showing that the mutation indeed led to mRNA mis-splicing (Figure 1E). We also detected two other mRNA isoforms, one derived from the activation of an upstream 3′ splice site in intron 6 causing a 39-bp intron retention (SV2), and the other causing 12-bp intron retention and a 39-bp truncation involving partial exons 7 and 8 (c.757-c.795) (SV3) (Figure 1E). SV2 and SV3 only accounted for the 4% of total mRNAs (Figure 1E). Aberrant *SARS2* transcripts were not detected in a healthy control sample. Therefore, the c.654–14T > A variant caused aberrant mRNA splicing, and SV1 was further investigated because of its overwhelming abundance. Translation of SV1 resulted in the *SARS2* K218R mutation plus an insertion of four amino acids (NLSP) between positions Q217 and R218 (Figure 1F, Supplementary Figure S1A). The SV1-encoded mutant was named Ins12. Class II SARS2 has three class-defining motifs in its active site (9,39) (Figure 1F, Supplementary Figure S1A). In the bovine SARS2 structure with serine adenylate (Ser-AMS) (PDB No. 1WLE) (19), a highly flexible loop in motif II (designated loop A), ranging from 329YRAETDTGKEPWGLYRVH346, extensively interacts with the adenosine moiety (Supplementary Figure S1A). Of note, a glycine at the tip of this loop, G341, uses its main chains to interact with side chain of Q217, which is in a spatially opposite loop (ranging from 217QKRLSHVSGHRSY229, designated loop B) (Figure 1F, Supplementary Figure S1A). In the Ins12 mutant, a four-amino acid peptide (NLSP) was inserted between Q217 and R218 (Figure 1F, Supplementary Figure S1A), likely causing loss of Q217-G341 interaction. The maternal *SARS2* c.1519dupC mutation led to a frameshifting and stop codon readthrough, replacing of the last 12 residues with an extended peptide of 40 amino acids (Figure 1E, F). The c.1519dupC-encoded mutant was named dupC.

Structural determination suggested Ins12 and dupC exhibited defects in dimerization and tRNA binding

To understand the potential effects of mutations on the structure, we crystallized the N-terminal Met^{1}-Val^{180}-truncated SARS2 and Ins12 (Supplementary Table S2). Full-length proteins could not be crystallized, nor could full-length or truncated dupC. In wild-type and Ins12 crystal structures, the electron densities of a few regions, including 218–227, 263–301, 331–340 and 495–518 residues, were untraceable (Supplementary Figure S1B). Where the crystal structures were defined, Ins12 showed a very similar structure to the wild-type, with a root-mean-square deviation (RMSD) as low as 0.177 Å (over 209 Cα atoms). In addition, both wild-type and Ins12 showed high similarity to the bovine SARS2 structure (PDB No. 1WLE) (19), with RMSD values of 0.442 Å (over 203 Cα atoms) and 0.383 Å (over 198 Cα atoms), respectively (Supplementary Figure S1B). These results indicate that the Ins12 mutation altered the local, rather than global, structure of SARS2.

Because the Ins12 mutation occurs in loop B, which lacks electron density, we could not directly compare it with the wild-type protein from the determined structures. Therefore, we developed structural models of SARS2, Ins12, and dupC using AlphaFold (40,41). The calculated models of wild-type and Ins12 fit very well onto the determined crystal structures, with RMSD values of 0.470 Å (over 200 Cα atoms) and 0.421 Å (over 210 Cα atoms) (Supplementary Figure S1C, D), respectively, indicating high confidence of the models. The AlphaFold-calculated structures reveals that the Ins12 mutation is located at the dimer interface. The peptide insertion enlarged the original loop B and may introduce an extra steric hindrance for SARS2 dimerization (Supplementary Figure S1E). In addition, loop A is located on the opposite side of the mutation site and is essential for ATP binding (Supplementary Figure S1E). To further study the effect of the Ins12 mutation on tRNA binding, we superimposed AlphaFold models onto the *Thermus thermophilus* SerRS-tRNA structure (PDB No. 1SER) (39). In wild-type SARS2, K218 was close to the tRNA base 67. The substitution of K218 with the extended loop 'NLSPR' may cause a clash with tRNA at bases 67 and 68 (Supplementary Figure S1F). Therefore, the Ins12 mutation may have affected dimerization and substrate-binding.

Similarly, we superimposed the dupC model onto the SARS2 dimer model and *T. thermophilus* SerRS-tRNA structure (PDB No. 1SER) (39) (Supplementary Figure S1G). The region with replacement and extension of the C-terminus in dupC was predicted to be a long loop, likely oscillating over a large space in solution and potentially interfering with SARS2 dimerization and tRNA binding (Supplementary Figure S1G).

Ins12 was defective in homodimerization

We ectopically expressed genes encoding C-terminal Myc-tagged SARS2 (SARS2-Myc), Ins12 (Ins12-Myc) and dupC (dupC-Myc) in HEK293T cells. The steady-state protein abundance of both Ins12-Myc and dupC-Myc was significantly lower than that of wild-type SARS2-Myc (Figure 1G). No obvious protein aggregates were observed for Ins12-Myc or dupC-Myc, indicating their relatively stable structures *in vivo*. Moreover, the CHX chase assay revealed that the *in vivo* stability of both mutants was comparable with that of SARS2, suggesting that decreased amounts of Ins12-Myc and dupC-Myc were not attributable to accelerated protein degradation (Figure 1H). Immunofluorescence analysis using anti-Myc suggesting that the two mutations did not influence proper cellular localization (Supplementary Figure S2).

Dimerization of class II SARS2 is required for tRNA aminoacylation (9,10). The capacity of Ins12 and dupC to form homodimers or heterodimers *in vivo* was also determined. Three proteins, dupC, Ins12, and wild-type SARS2 (encoded by the paternal c.654–14T > A allele), co-existed in the patient cells. Genes encoding C-terminal FLAG-tagged SARS2 (SARS2-FLAG), Ins12 (Ins12-FLAG), or dupC (dupC-FLAG) were co-expressed with genes encoding SARS2-Myc, Ins12-Myc, or dupC-Myc in HEK293T cells. Co-immunoprecipitation (Co-IP) analysis clearly showed that homo- or heterodimerization between SARS2-FLAG/dupC-Myc, SARS2-FLAG/Ins12-Myc, and dupC-FLAG/Ins12-Myc was not obviously impaired while homodimerization between dupC-FLAG/dupC-Myc was in

Table 1. Binding affinities of SARS2, Ins12 and dupC for hmtRNA^{Ser}(AGY) and hmtRNA^{Ser}(UCN)

enzyme	tRNA	K_D (μM)	k_{on}*10^2 (μM^{-1}s^{-1})	k_{off} *10^4 (s^{-1})	Fold/SARS2
SARS2	hmtRNA^{Ser}(AGY)	0.03 ± 0.01	2.55 ± 0.03	7.77 ± 0.08	1
Ins12		0.11 ± 0.01	0.82 ± 0.01	8.79 ± 0.05	∼3.7
dupC		0.33 ± 0.03	0.16 ± 0.01	5.29 ± 0.04	11
SARS2	hmtRNA^{Ser}(UCN)	0.08 ± 0.01	1.22 ± 0.01	9.43 ± 0.04	1
Ins12		0.08 ± 0.01	1.08 ± 0.01	8.69 ± 0.05	1
dupC		0.28 ± 0.02	0.22 ± 0.01	6.17 ± 0.04	3.5

Mean ± SD, $n = 6$.

Table 2. Kinetics of SARS2, Ins12 and dupC for Ser and ATP in ATP-PPi exchange reaction

Enzyme	Substrate	K_m [mM (Ser), μM (ATP)]	k_{cat} (s^{-1})	k_{cat}/ K_m (μM^{-1}min^{-1})	Relative k_{cat}/ K_m (%)
SARS2	Ser	2.40 ± 0.04	2.11 ± 0.03	0.88	100
Ins12		1.66 ± 0.03	0.98 ± 0.02	0.59	67
dupC		1.28 ± 0.08	1.88 ± 0.07	1.47	167
SARS2	ATP	112.83 ± 10.54	1.87 ± 0.05	16.57	100
Ins12		64.69 ± 4.48	0.91 ± 0.01	14.07	84.9
dupC		61.37 ± 2.20	1.50 ± 0.03	24.44	147.5

Mean ± SD, $n = 3$.

fact even higher; however, homodimerization of Ins12-FLAG/Ins12-Myc was significantly decreased (Figure 1I). This observation was consistent with the results of AlphaFold-based Ins12 model (Supplementary Figure S1E) and the fact that loop B directly mediates dimer formation (19).

We have successfully purified mature SARS2 from *E. coli* (32,33). We obtained mature forms of wild-type, Ins12, and dupC, and then performed thermal shift assays (TSA) to determine the stability of purified proteins *in vitro* (42). The apparent melting temperature (Tm) value of dupC (54.0°C) was comparable with that of SARS2 (54.2°C); however, that of Ins12 (52.1°C) was lower, suggesting a more relaxed conformation in solution (Figure 1J).

The above data showed that the two mutants displayed a decreased steady-state abundance when overexpressed, without impairment of *in vivo* stability or mitochondrial localization. Furthermore, homodimerization of Ins12 was impaired, implying a reduction in tRNA aminoacylation.

SARS2 mutants exhibited weakened tRNA binding capacities and abolished or impaired tRNA charging activities at the aminoacylation level

We determined the tRNA-binding affinity of SARS2 and the two mutants by measuring K_D values. Ins12 and SARS2 exhibited the same K_D value (0.08 μM) for hmtRNA^{Ser}(UCN); however, that of dupC was evidently elevated (0.28 μM) (Table 1). For tRNA^{Ser}(AGY), the K_D value of Ins12 increased approximately 3.7-fold, and that of dupC increased approximately 11-fold. These data suggest that Ins12 exhibited an impaired tRNA binding affinity for tRNA^{Ser}(AGY), whereas dupC displayed dramatically impaired binding for both tRNAs, highlighting the crucial role of the C-terminus in tRNA binding (19). Alteration in K_D values was mainly derived from k_{on} constants. Furthermore, the different effects of Ins12 on binding between the two tRNAs suggested that their acceptor ends were differently accommodated into the active site.

SARS2 activates Ser and transfers it to tRNA^{Ser}s. Amino acid activation kinetics in ATP-PPi exchange reactions (Table 2) showed that both mutants exhibited simultaneous decreases in K_m and k_{cat} values for ATP and Ser, suggesting that local structural rearrangement altered ATP and Ser binding. The resultant catalytic efficiency (k_{cat}/ K_m) of dupC for both substrates was not negatively impaired; however, that of Ins12 was slightly decreased. The aminoacylation kinetics (Table 3) showed that those of Ins12 for both hmtRNA^{Ser}(AGY) and hmtRNA^{Ser}(UCN) were too low to be determined accurately. Meanwhile, For hmtRNA^{Ser}(AGY), dupC exhibited a nearly 6-fold increase in K_m and 3-fold decrease in k_{cat}, leading to only ∼5% activity when compared with that of SARS2. For hmtRNA^{Ser}(UCN), the catalytic efficiency of dupC decreased by ∼60% due to an increase in K_m and a decrease in k_{cat}, although the changes were less pronounced than those for hmtRNA^{Ser}(AGY).

Together, these data showed that both Ins12 and dupC, particularly the latter, exhibited impaired tRNA binding capacities. In addition, both mutants displayed abolished or impaired tRNA aminoacylation activity *in vitro*.

A significant decrease in hmtRNA^{Ser}(AGY) due to selective degradation impaired mitochondrial mRNA translation in patient cells

To understand whether these two mutations could affect mitochondrial translation *in vivo*, we constructed four lines of iPSCs (Supplementary Figure S3) using peripheral blood samples from the patient, her parents, and a healthy control (28).

We raised an antibody against SARS2 using purified SARS2 as the antigen. The steady-state level of SARS2 was detected, showing that dupC, with its large molecular mass, could be readily detected in both patient and maternal samples in comparable levels. The abundance of Ins12 and/or SARS2 (indistinguishable in size) was dramatically reduced in patient cells when compared with SARS2 from other

Table 3. Kinetics of SARS2, Ins12 and dupC for hmtRNA^{Ser}(AGY) and hmtRNA^{Ser}(UCN) in aminoacylation

Enzyme	tRNA	K_m (μM)	k_{cat} (min^{-1})	k_{cat}/K_m ($\mu M^{-1}min^{-1}$)	Relative k_{cat}/K_m (%)
SARS2	hmtRNA^{Ser}(AGY)	1.03 ± 0.07	1.71 ± 0.06	1.66	100
Ins12		ND	ND		
dupC		5.76 ± 1.12	0.51 ± 0.04	0.09	5.4
SARS2	hmtRNA^{Ser}(UCN)	0.82 ± 0.27	0.87 ± 0.04	1.06	100
Ins12		ND	ND		
dupC		1.27 ± 0.37	0.53 ± 0.10	0.42	39.6

ND, not accurately determined due to low activity. Mean ± SD, $n = 3$.

three cells (Figure 2A). Maternal cells harbored a wild-type or a mutant allele in each chromosome; however, the level of dupC was only ∼6.3% that of wild-type SARS2 (Figure 2A).

We then compared the steady-state abundance of hmtRNA^{Ser}(AGY) and hmtRNA^{Ser}(UCN) in various cell lines using northern blot and found that level of hmtRNA^{Ser}(AGY) was obviously decreased to approximately 25% in patient cells when compared with that in control cells (Figure 2B). However, the level of hmtRNA^{Ser}(UCN) was not significantly different between samples. Furthermore, the amounts of noncognate hmtRNA^{Thr} and hmtRNA^{Leu}(UUR), transcribed from the same H-strand as hmtRNA^{Ser}(AGY), were similar between patient and control cells, suggesting that hmtRNA^{Ser}(AGY) in patient cells was rapidly degraded (Figure 2B). The steady-state of hmtRNA^{Ser}(AGY) in four iPSCs was monitored in the presence of ethidium bromide (EB), a mitochondrial transcription inhibitor (43,44). The results showed a significantly shortened lifespan of hmtRNA^{Ser}(AGY) in patient-derived iPSCs compared to that in other samples (Figure 2C). The half-life of patient hmtRNA^{Ser}(AGY) was estimated to be approximately 5.5 h, whereas that in other three cells was over 20 h. We therefore concluded that the abnormal decrease in patient hmtRNA^{Ser}(AGY) was due to the high degradation rate.

Aminoacylation levels of hmtRNA^{Ser}(AGY) and hmtRNA^{Ser}(UCN) were determined under acidic conditions to preserve the labile bond between Ser and A76. Results showed that hmtRNA^{Ser}(UCN) charging was not markedly influenced, whereas charging of residual hmtRNA^{Ser}(AGY) in patient cells was slightly but significantly lower than that in other cell lines (Figure 2D). Furthermore, aminoacylation of the noncognate hmtRNA^{Thr} and hmtRNA^{Leu}(UUR) was consistent across samples (Figure 2D). Both the reduced amount and aminoacylation level of hmtRNA^{Ser}(AGY) suggested impaired mitochondrial translation. Indeed, the levels of both mitochondrial DNA (mtDNA)-encoded MT-ND3 (complex I (CI) component) and MT-ATP8 (CV component) were significantly lower in patient cells than in other samples (Figure 2E). However, the levels of MT-ND1 (CI component), MT-CYB (CIII component), MT-CO1 (CIV component), and MT-ATP6 (CV component) were comparable. Considering no AGY codon in MT-ATP8, we suggested that its lower amount was an indirect effect of dysfunctional mitochondrial translation in patient cells. We further performed quantitative reverse transcription PCR (RT-PCR) to detect the transcript level of the mtDNA-encoded mRNAs, revealing comparable amounts of various mRNAs and suggesting impaired mRNA translation, but not transcription (Supplementary Figure S4).

To investigate potential defects in mitochondrial translation caused by *SARS2* variants, iPSCs were pulse-labeled with [^{35}S]-methionine and [^{35}S]-cysteine and nDNA translation was blocked with emetine. The overall rate of mitochondrial translation in patient cells was apparently higher than that in other cells (Figure 2F). The iPSCs were then pulse-labeled and chased for 18 h to detect the degradation rate of mitochondrial translation products. The results showed that remaining signals of [^{35}S]-labelled proteins in patient cells were weaker than those in other samples, indicating a shorter half-life of mitochondrial translation products (Figure 2F). This suggests that, although the mitochondrial translation rate was higher in patient cells, possibly due to a compensatory effect, its protein products were unstable and prone to degradation.

The above data suggest that, in patient cells, it had a dramatically decreased abundance of SARS2 (or its mutants) and hmtRNA^{Ser}(AGY) due to rapid selective degradation. In combination with the impaired tRNA aminoacylation activity of the mutants, Ser-hmtRNA^{Ser}(AGY) was sharply reduced and mitochondrial translation was impaired.

Patient cells exhibited reduced complex I activity and respiratory capacity

Comparable levels of mtDNA-replication and transcription-related POLG2 and TFAM (45), other mito-aaRSs (AARS2, IARS2, KARS, NARS2 and TARS2) (12) and protein trafficking-associated TOM40 and TIM23 (46), were observed among four cells (Supplementary Figure S5), indicating two mutations had little effect on mitochondrial biogenesis.

OXPHOS complexes are of dual origin (47). In patient cells, a reduced abundance of NDUFS1 (in CI) and UQCRC2 (in CIII) was observed; however, that of SDHA and SDHB in CII, which harbors only nDNA-encoded members, was consistent. In addition, normal level of NDUFS2 (CI component) or ATP5A1 (CV component) was observed in patient cells, suggesting selective downregulation of OXPHOS components (Figure 2G).

Activities of CI-CIV determination revealed that CI activity in patient was significantly lower than that in all other samples, whereas the activities of CII-CIV in patient were not consistently lower than those of other cell lines (Figure 3A).

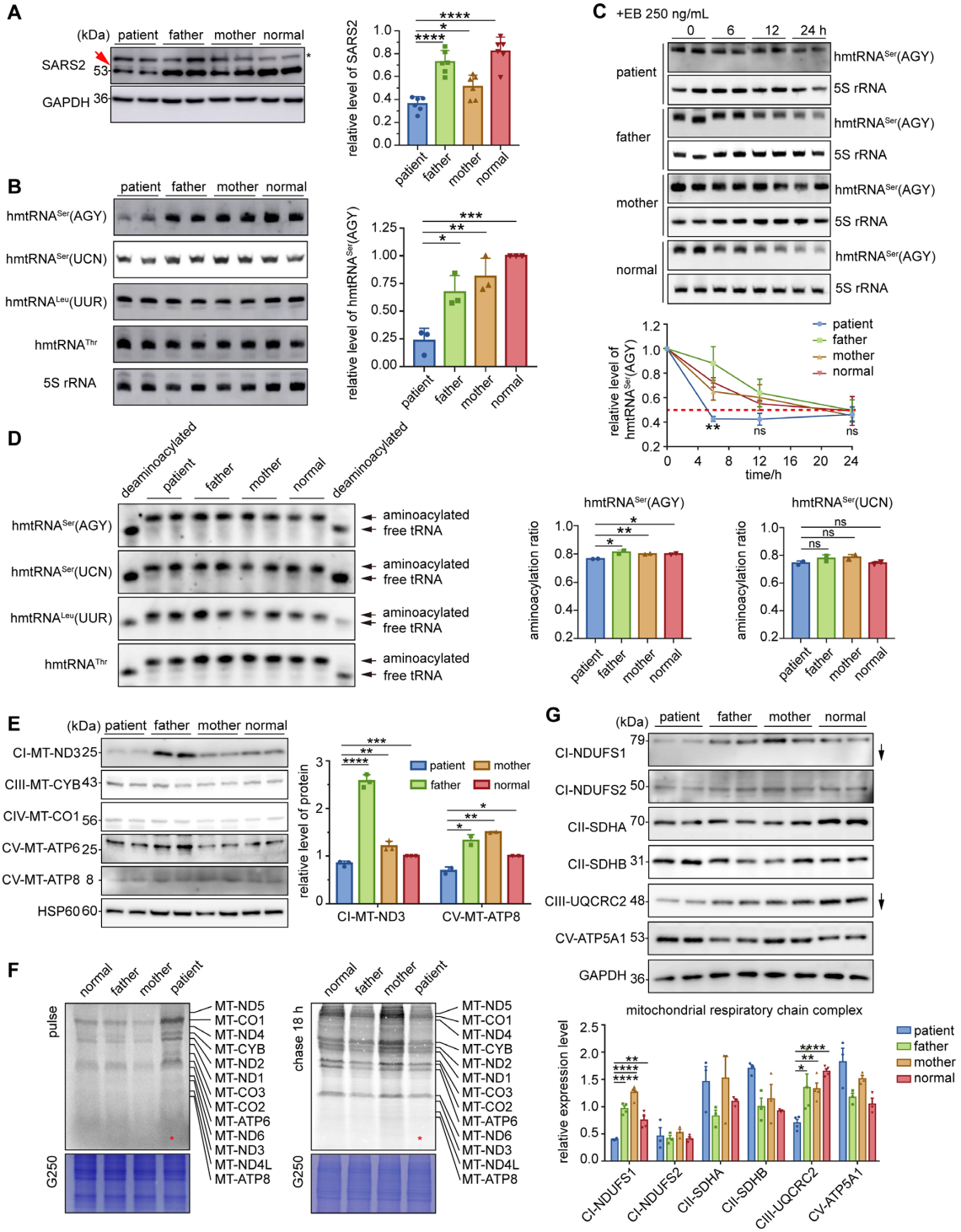

Figure 2. *SARS2* mutations led to decreased hmtRNA^{Ser}(AGY) due to selective degradation and a reduction of specific OXPHOS components. (**A**) Expression of SARS2 in four iPSCs. dupC was indicated with a red arrow; a non-specific band was indicated by an asterisk. The band intensities were measured and normalized to those of GAPDH (right panel). (**B**) Steady-state abundance of mitochondrial tRNAs detected by northern blot; 5S rRNA was used as the loading control. The data were normalized to those of normal control iPSCs. (**C**) iPSCs were treated with EB for the indicated time points. Northern blot was performed to detect steady-state abundance of hmtRNA^{Ser}(AGY). The band intensity was measured, normalized to 5S rRNA, and plotted as a percentage of the initial band intensity (lower panel). The asterisks showed statistical differences between patient and normal control iPSCs. (**D**) Aminoacylation level of mitochondrial tRNAs determined by acidic northern blot. The proportion of aminoacylated hmtRNA^{Ser}s is quantified (right panels). (**E**) Western blot analysis of mtDNA-encoded mitochondrial proteins. HSP60 was used as a loading control. The expression of mtDNA-encoded mitochondrial proteins was normalized to that of controls (right panel). (**F**) Pulse-chase analysis showing synthesis (pulse) and stability (chase) of mtDNA-encoded proteins. The lane of the patient is indicated with a red asterisk. The loaded volume was normalized by G250 staining. (**G**) Western blot analysis of nDNA-encoded mitochondrial proteins. The band intensities were measured and normalized to those of GAPDH (lower panel). Values are expressed as mean ± SD ($n = 2$–6). P indicates significance according to the unpaired two-tailed t-test. *$P < 0.05$, **$P < 0.01$, ***$P < 0.001$, ****$P < 0.0001$.

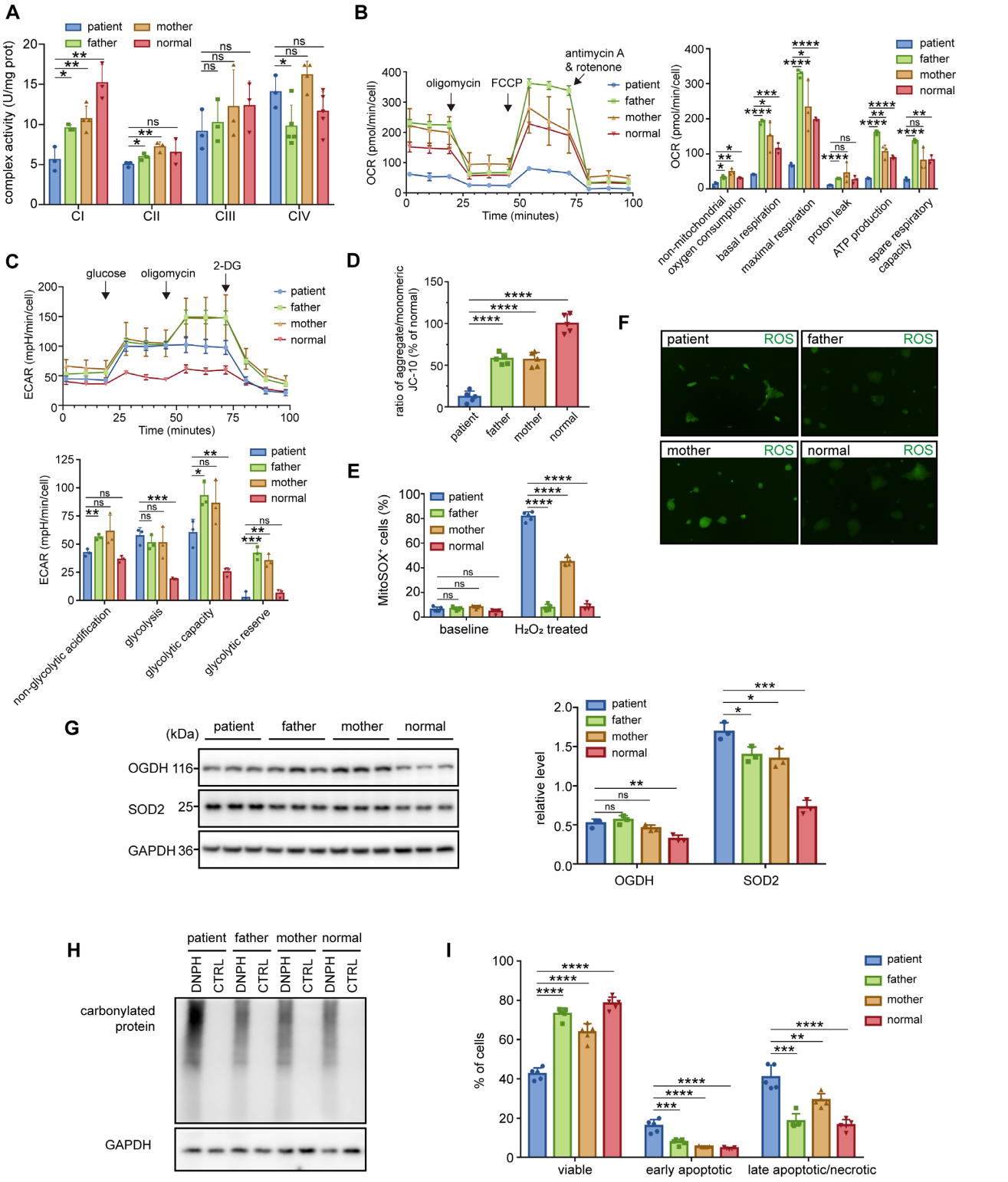

Figure 3. Multiple mitochondrial dysfunctions caused by *SARS2* mutations. (**A**) Activities of CI-CIV from mitochondria isolated from various iPSCs. (**B**) OCR, as determined with inhibitors including oligomycin, FCCP, antimycin A, and rotenone. The results of non-mitochondrial, basal, maximal, proton leak, ATP production respiration, and spare respiratory capacity OCR were normalized by cell count. (**C**) ECAR, as determined with glucose, oligomycin, and 2-Deoxy-D-glucose (2-DG). The results of non-glycolysis, glycolysis, glycolytic capacity, and glycolytic reserve ECAR were normalized by cell count. (**D**) MMP, measured using the fluorescence probe JC-10 assay system. (**E**) ROS levels detected using MitoSOX with or without H_2O_2 stimulation. (**F**) Fluorescent micrographs showing intracellular ROS formation, as indicated by DCFH-DA staining. (**G**) Western blot analysis of OGDH and SOD2. The band intensities were measured and normalized to those of GAPDH (right panel). (**H**) Level of protein carbonylation in various iPSCs. (**I**) Apoptosis levels of various iPSCs. Values are expressed as mean ± SD ($n = 3$–5). P values were determined by unpaired two-tailed t-tests. $^{*}P < 0.05$, $^{**}P < 0.01$, $^{***}P < 0.001$, $^{****}P < 0.0001$; ns, not significant. The results are representative of at least two independent experiments.

Subsequently, to evaluate whether the mutations affected energy production, we examined the oxygen consumption rates (OCR) of all four iPSC lines. The basal OCR, ATP production OCR, proton leak OCR, maximal respiration OCR, spare respiratory capacity, and nonmitochondrial oxygen consumption in patient were significantly lower (Figure 3B). Collectively, these results showed that patient OXPHOS function and energy production were affected by the two mutations.

We also measured the extracellular acidification rate (ECAR) of the iPSCs. The non-glycolytic acid levels were similar across cell types. Lifting of ECAR was observed after the addition of glucose. The increase in extracellular acidification levels in patient cells was higher than that in the control cells. The glycolytic capacity of patient cells was close to that of paternal and maternal cells, but reached 3-fold that of control cells in the presence of oligomycin. Glycolysis in patient cells was similar with that in parent cells, but stronger than that of the control cells (Figure 3C). These results reflected the damaged glycolytic capacity and reserve in patient cells.

A normal membrane potential (MMP) is a prerequisite for producing ATP (48). Flow cytometry results indicated that the MMP of parent-derived cells was ∼40% lower than that of the control, whereas MMP of patient-derived cells was 87.5% lower than that of the control (Figure 3D). This suggests that parental cells exhibited a certain degree of mitochondrial depolarization.

High ROS levels were generated in patient-derived iPSC cells

We analyzed the level of superoxide, a representative ROS, in various iPSCs using the mitochondrial superoxide indicator mitoSOX. The results showed that, in a basic environment, levels of superoxide free radicals among the four cell lines were almost identical, with only slightly high levels in patient- and mother-derived cells (Figure 3E). After treatment with H_2O_2, the superoxide content in patient cells obviously increased (Figure 3E). Superoxide levels in maternal cells also increased noticeably in the presence of H_2O_2. ROS production, as detected by the fluorescence intensity, in patient and maternal cells was slightly higher than other two cells (Figure 3F). Western blot results showed that levels of the ROS scavenging–related protein, SOD2 (49), was significantly elevated in patient cells. However, no significant difference in the level of ROS production-related proteins, such as OGDH (50), was observed among the four cells (Figure 3G), implying that ROS were mainly produced by perturbed electron transport. Analysis of protein carbonylation, mediated by excessive ROS (51), showed that protein carbonylation level in patient-derived iPSCs was apparently higher than that in other cell lines (Figure 3H).

Based on higher ROS and lower MMP in the patient cells, we further investigated the apoptosis level. Both the early apoptotic and late apoptotic or necrotic cell populations increased significantly, whereas the level of viable cells was lower in the patient-derived iPSCs. A slight increase in the number of late apoptotic or necrotic cells and a slight decrease in the number of viable cells were also observed in maternally-derived cells (Figure 3I).

The two mutations led to change in mitochondrial dynamics and activated mitophagy

We further compared the amount of several key regulators during mitochondrial dynamics, including DRP1 (for mitochondrial division) (2), MFN1, and MFN2 (for mitochondrial fusion) (1). Abundance of both DRP1 and MFN2 was notably decreased in patient cells; MFN1 levels were comparable between iPSCs from the patient, maternal, and control cells, but higher in paternal cells (Figure 4A). Mitochondria in various iPSCs were further observed via transmission electron microscopy (TEM) (Figure 4B). In the cytoplasm of paternal, maternal, and control cells, mitochondria presented a clear and dense double-membrane structure with visible, inwardly folded cristae structures and a round, oval, or elongated stick-shaped appearance. In patient cells, however, many mitochondria were swallowed likely by autophagosomes or autolysosomes, and the inner membrane structure was destroyed, with disordered vacuoles (Figure 4B). These differences indicate that mitochondrial morphology was affected by impairments in fusion and/or fission processes.

Due to the observed potential autophagosomes, we further detected the mitophagy (52). No significant difference was observed in LC3 II/I levels between the four cell lines, but patient cells exhibited significantly lower p62 levels than other samples (Figure 4C). Considering that LC3II may be depleted by autophagy-lysosomal degradation, the levels of LC3II/I and p62 were further analyzed after the cells were treated with an autophagy inhibitor bafilomycin A1 (Baf A1) (53). The results of the autophagy flux assay revealed significantly increased LC3II and p62 levels in patient iPSCs, suggesting a high abundance of autophagosomes and an active autophagic flux in patient cells (Figure 4D). Examination of mitochondrial autophagy-related protein levels among cells showed that both Parkin and BCL2L13 levels in patient cells were significantly higher than other cells (Figure 4E), indicating that both Parkin-dependent (4) and-independent (5) mitophagy were activated.

Overexpression of wild-type *SARS2* rescued the comprehensive defects in patient-derived iPSCs

To understand whether *SARS2* malfunction is the predominant driver for the above pleiotropic effects, we stably expressed the wild-type *SARS2* in patient-derived iPSCs and obtained a cell line referred to as P-WT. *SARS2* was more expressed in P-WT cells than in the other four iPSCs (Figure 5A).

We investigated whether the sharp decrease in patient hmtRNA^{Ser}(AGY) levels could be reversed. A remarkable increase (3–4-fold) in the steady-state level of hmtRNA^{Ser}(AGY) was observed in P-WT, reaching a level comparable to that in other cells (Figure 5B). No significant changes were seen in the steady-state levels of hmtRNA^{Ser}(UCN), hmtRNA^{Thr}, or hmtRNA^{Leu}(UUR), suggesting a specific effect of *SARS2* variants on hmtRNA^{Ser}(AGY) abundance. The steady-state level of hmtRNA^{Ser}(AGY) in P-WT remained consistent over 24 h and was more stable than that in maternal cells, indicating that *SARS2* overexpression protected

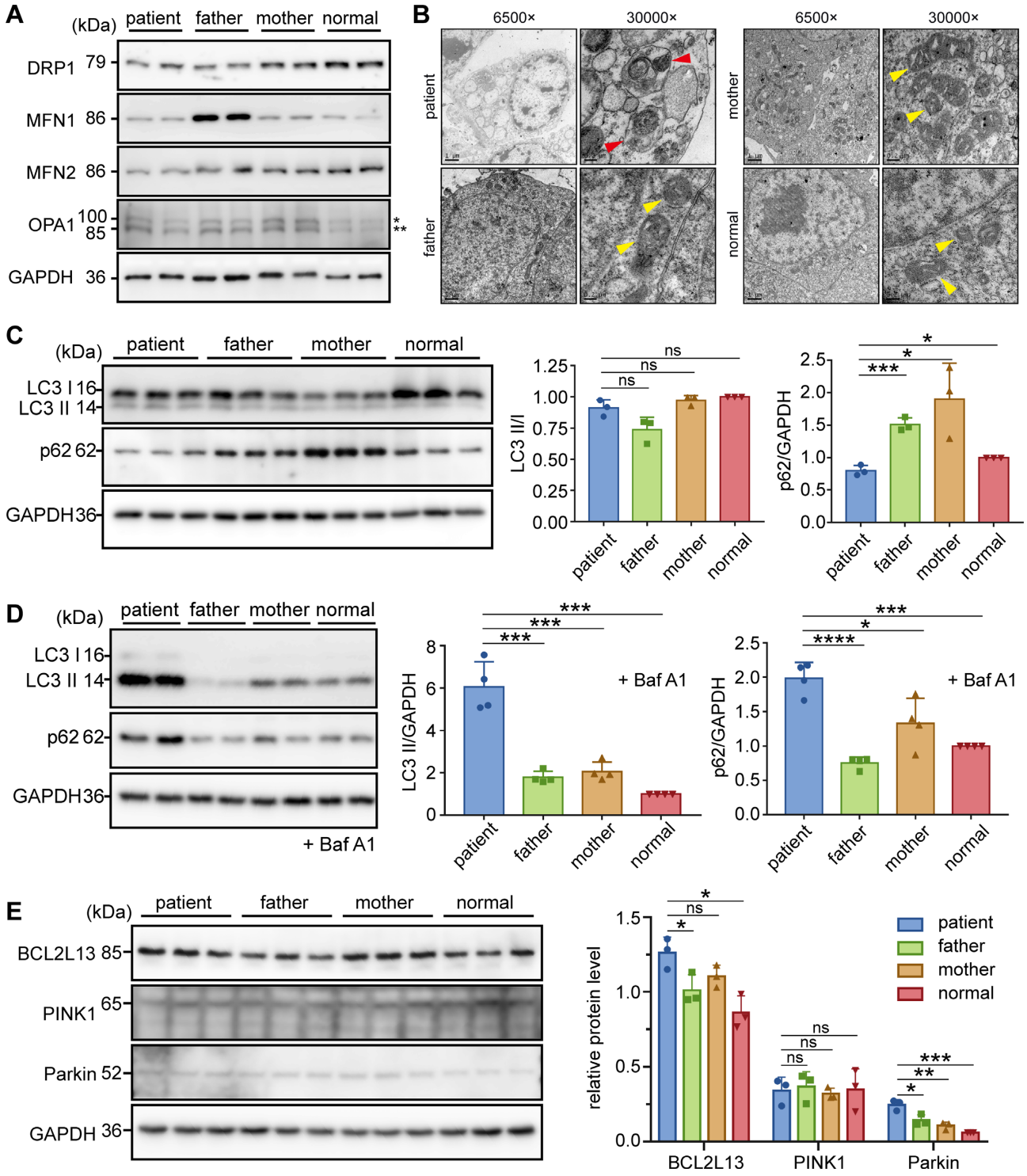

Figure 4. Aberrant mitochondrial dynamics and activated mitophagy and in patient cells. (**A**) Protein levels of DRP1, MFN1, MFN2 and OPA1 (two forms indicated with one or two asterisks) in four iPSCs. GAPDH was used as a loading control. (**B**) Mitochondria in various iPSCs were observed by TEM. Red arrowheads indicate autophagolysosomes in patient iPSCs. Yellow arrowheads indicate normal mitochondria. (**C, D**) Western blot analysis of LC3 and p62 with or without Baf A1. GAPDH was used as a loading control. The LC3 II/I ratio and the levels of p62 and LC3 II were calculated and normalized to those of the normal control (right panels). (**E**) Western blot analysis of BCL2L13, PINK1, and Parkin. The band intensities were measured and normalized to those of GAPDH (right panel). Values are expressed as mean ± SD ($n = 3$–4). P values were determined by unpaired two-tailed t-tests. $^{*}P < 0.05$, $^{**}P < 0.01$, $^{***}P < 0.001$, $^{****}P < 0.0001$; ns, not significant.

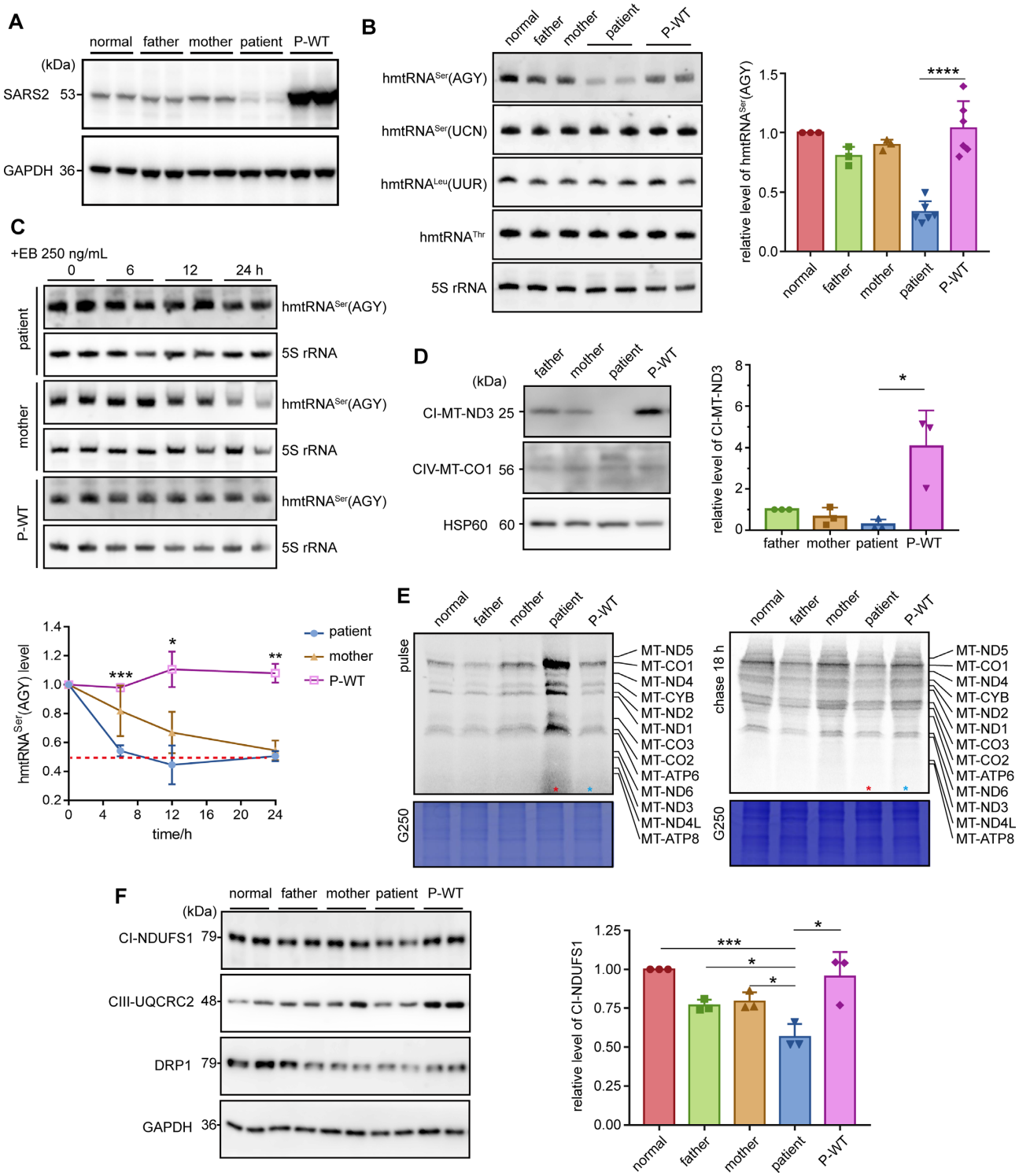

Figure 5. Overexpression of the wild-type *SARS2* rescued hmtRNA^{Ser}(AGY) levels and corrected mitochondrial translational defects. (**A**) Expression of SARS2 in iPSCs, as detected by western blot assay using anti-SARS2 antibody. GAPDH was used as a loading control. (**B**) Steady-state abundance of mitochondrial tRNAs detected by northern blot; 5S rRNA was used as the loading control. Data were normalized to those of normal control iPSCs (right panel). (**C**) iPSCs were treated with EB for the indicated time points. Northern blot was performed to detect steady-state abundance of hmtRNA^{Ser}(AGY). The band intensity was measured, normalized to 5S rRNA, and plotted as a percentage of the initial band intensity (lower panel). The asterisks showed statistical differences between P-WT and patient iPSCs. (**D**) Western blot analysis of mtDNA-encoded MT-ND3 and MT-CO1. The band intensities were measured and normalized to those of HSP60 (right panel). (**E**) Synthesis and stability of mtDNA-encoded proteins, as determined by pulse-chase analysis. The lane of the patient is indicated with a red asterisk. The lane of P-WT is denoted by a blue asterisk. The loaded volume was normalized by G250 staining. (**F**) Expression of NDUFS1, UQCRC2, and DRP1, as detected by western blot. GAPDH was used as a loading control. Data were normalized to those of normal control iPSCs (right panel). Values are expressed as mean ± SD ($n = 3$–6). *P* indicates significance according to the unpaired two-tailed *t*-test. *$P < 0.05$, **$P < 0.01$, ***$P < 0.001$, ****$P < 0.0001$.

against and effectively reversed the physiological degradation of hmtRNA^{Ser}(AGY) in patient cells (Figure 5C). hmtRNA^{Ser}(AGY) in P-WT was efficiently aminoacylated. Because the hmtRNA^{Ser}(AGY) in patient-derived iPSCs was highly aminoacylated, the difference in aminoacylation level between patient and P-WT cells was not significant (Supplementary Figure S6). These data clearly show that the replenished hmtRNA^{Ser}(AGY) in P-WT was readily charged. Aminoacylation levels of hmtRNA^{Ser}(UCN), hmtRNA^{Thr}, or hmtRNA^{Leu}(UUR) between samples were comparable (Supplementary Figure S6).

MT-ND3 level was recovered in P-WT (Figure 5D), suggestive of restored mitochondrial mRNA translation. Pulse-chase experiments showed that the mitochondrial translation rate in P-WT was comparable to that in parental and control cells. Moreover, mtDNA-encoded protein stability in P-WT was similar with that in parental and control cells, as evidenced by a higher proportion of products remaining stable than that in patient cells (Figure 5E). These data suggest that SARS2 replenishment rescued the mitochondrial translation dysfunction in patient cells.

NDUFS1 (in CI) was significantly reduced in patient cells, but increased by ∼2 fold in P-WT to a level comparable to that in other cells (Figure 5F). In addition, steady-state levels of UQCRC2 (in CIII) and DRP1 were evidently increased in P-WT after SARS2 replenishment (Figure 5F). The above results suggest that abnormal levels of nDNA-encoded mitochondria-related proteins in patient cells were associated with *SARS2* variants.

The CI activity of P-WT reached a level close to that of the healthy control and was more than 1.5-fold that in patient iPSCs (Figure 6A). Meanwhile, the activity of CII-CIV in P-WT was also greatly improved (Figure 6A), despite a lack of obvious impairment between the patient and control cells. Consistently, the respiratory activity of P-WT was also improved compared to that of the patient cells. The basal, proton leak, maximal respiration, non-mitochondrial, and ATP production OCR values in P-WT were comparable to control levels (Figure 6B). However, the spare respiratory capacity of P-WT was close to that of patient cells. Rising glycolysis and impaired glycolytic reserve could be apparently improved by expressing *SARS2*. The ECAR in P-WT decreased considerably after *SARS2* overexpression (Figure 6C), resembling that in healthy controls. Remarkably, the damaged glycolytic reserve seen in patient cells was efficiently repaired in P-WT. The protein carbonylation level in P-WT dropped significantly to a level close to that of the control cells (Figure 6D).

Autophagy flux experiments showed that, after Baf A1 treatment, the LC3II and p62 levels of P-WT were significantly lower than those in patient cells, reaching only ∼20% and ∼30% of the previously recorded levels and approaching the levels in parental and control cells (Figure 6E). These results indicate that SARS2 replenishment successfully rescued active autophagy in patient cells.

The morphology of the mitochondria in P-WT and patient cells was compared using TEM. Clear and dense mitochondrial double-layer membrane structures were observed in P-WT, and the number of vesicle structures, autophagosomes, and autolysosomes in P-WT cells was lower than that in patient cells (Figure 6F), suggesting that SARS2 effectively rescued abnormal mitochondrial morphology.

Ins12 and dupC mutations caused embryonic lethality in mice

To further understand whether either mutation impairs mitochondrial translation in model animals, we assessed the potential influence of these two mutations on mitochondrial tRNA^{Ser}(AGY) and translation in mice.

Due to the conservation of *SARS2* mRNAs between humans and mice, an allele carrying a dupC mutation was constructed by inserting a cytosine before c.1519C into the donor DNA fragment in the CRISPR/Cas9 system to yield heterozygous dupC mice (*Sars2*$^{dupC/+}$). Although c.654–13T (human c.654–14T counterpart) was present in the corresponding site in mouse *Sars2*, only 11 nucleotides (TCTGTCTCCAG) were immediately upstream of the splicing acceptor site of intron 6 (Supplementary Figure S7A), in contrast to the 12 nucleotides (TCTGTCTCCCAG) in human *SARS2*. If we directly constructed a c.654–13T > A knock-in mutation, we are not sure whether the introduced AG in *Sars2* could function as a splicing acceptor site as in human cells; the efficiency during splicing, even as an acceptor site, is unknown. Lastly and most importantly, after intron retention, the inclusion of 11 nucleotides would lead to frameshifting of the mutated mRNA and premature termination during translation. Based on these considerations, we constructed an Ins12 knock-in mouse (*Sars2*$^{Ins12/+}$) using CRISPR/Cas9 (Supplementary Figure S7B). RNA transcribed from this allele completely contained the mutant mRNA with 12 nucleotides (TCTGTCTCCCAG) between exons 6 and 7, without the wild-type version, and thus only translated the Ins12 mutant.

Mating between *Sars2*$^{Ins12/+}$ or *Sars2*$^{dupC/+}$ mice did not yield the corresponding homozygous offspring (*Sars2*$^{Ins12/Ins12}$ or *Sars2*$^{dupC/dupC}$) (Supplementary Table S3). Furthermore, we failed to obtain *Sars2*$^{Ins12/dupC}$ mice and *Sars2*$^{Ins12/dupC}$ embryos during the embryonic stage at E13.5 by mating *Sars2*$^{Ins12/+}$ and *Sars2*$^{dupC/+}$ mice (Figure 7A, Supplementary Table S3). This phenomenon demonstrated the embryonic lethality of *Sars2*$^{Ins12/dupC}$, *Sars2*$^{Ins12/Ins12}$ and *Sars2*$^{dupC/dupC}$ genotypes, suggesting that the survival of the human patient was related to the production of wild-type *SARS2* mRNA from the allele with c.654–14T > A variation.

Taken together, these observations demonstrated that Ins12 and dupC mutations impaired Sars2 function and were lethal to normal embryogenesis in mice *in vivo*.

Skeletal muscle from heterozygous mice exhibited lower mtRNA^{Ser}(AGY) and mtRNA^{Ser}(UCN) levels and impaired mitochondrial translation and morphology

We further analyzed mitochondrial translation and function in *Sars2*$^{Ins12/+}$ and *Sars2*$^{dupC/+}$ mice. Weight, length, and organ size of *Sars2*$^{Ins12/+}$ and *Sars2*$^{dupC/+}$ mice were not notably different from those of wild-type mice from birth to adulthood. Among energy-consuming tissues, western blot revealed obvious lower Sars2 levels in the heart and skeletal muscle (bilateral hindlimb) tissues of *Sars2*$^{Ins12/+}$ and

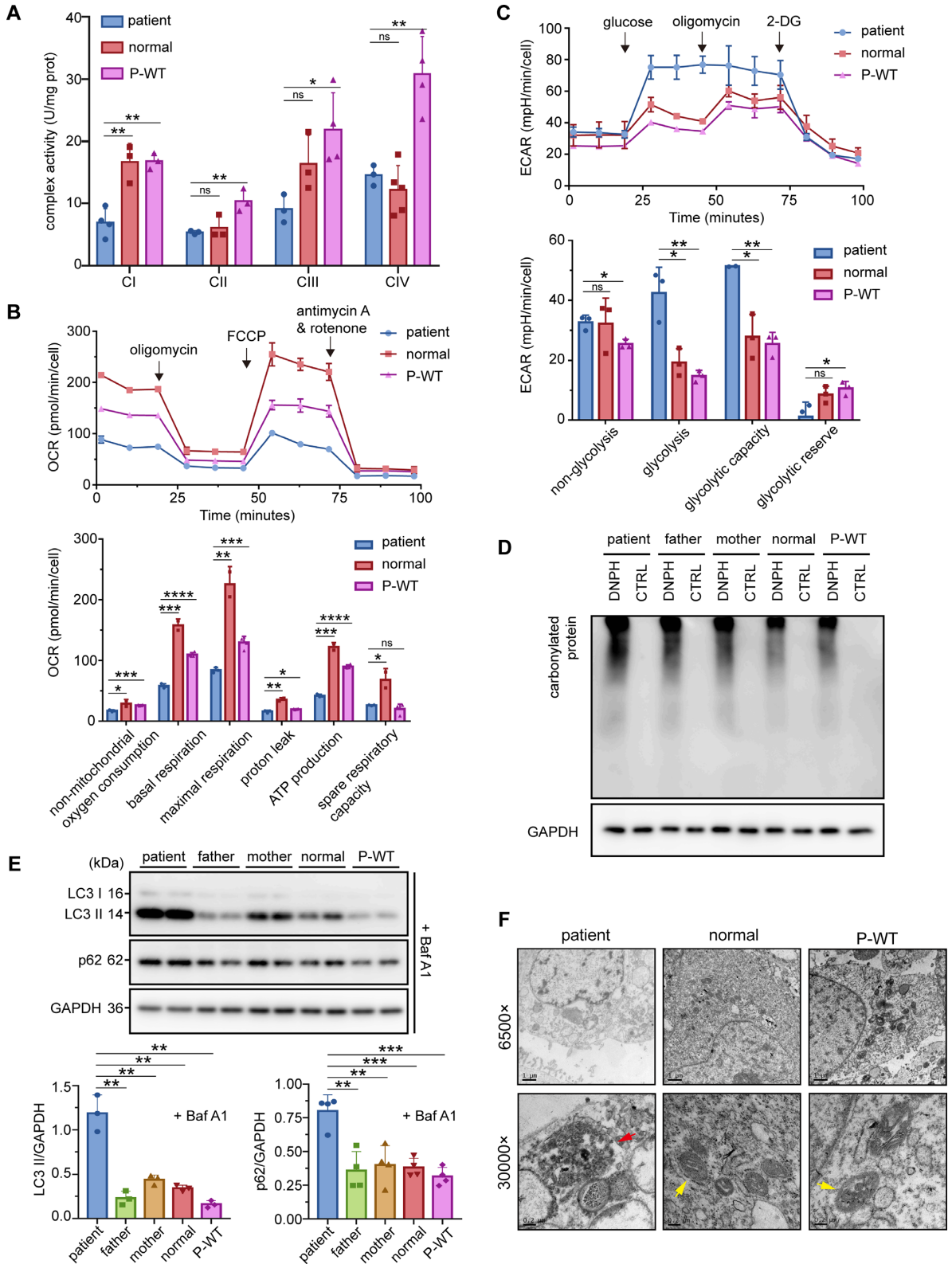

Figure 6. Mitochondrial malfunctions were rescued by overexpression of wild-type *SARS2*. (**A**) Activities of CI-CIV of various cell lines. (**B**) OCR determination of various cell lines. The results of non-mitochondrial, basal, maximal, proton leak, ATP production respiration, and spare respiratory capacity OCR were normalized by cell count. (**C**) ECAR determination of various cell lines. The results of non-glycolysis, glycolysis, glycolytic capacity, and glycolytic reserve ECAR were normalized by cell count. (**D**) The level of protein carbonylation was determined by western blot. GAPDH was used as a loading control. (**E**) Western blot analysis of LC3 and p62 with Baf A1. The band intensities were measured and normalized to those of GAPDH (lower panels). (**F**) Mitochondria in various iPSCs were observed by TEM. The red arrow indicates autophagolysosomes. The yellow arrow indicates morphologically normal mitochondria. Values are expressed as mean ± SD ($n = 3$–4). *P* indicates significance according to the unpaired two-tailed *t*-test. $^{*}P < 0.05$, $^{**}P < 0.01$, $^{***}P < 0.001$; ns, not significant.

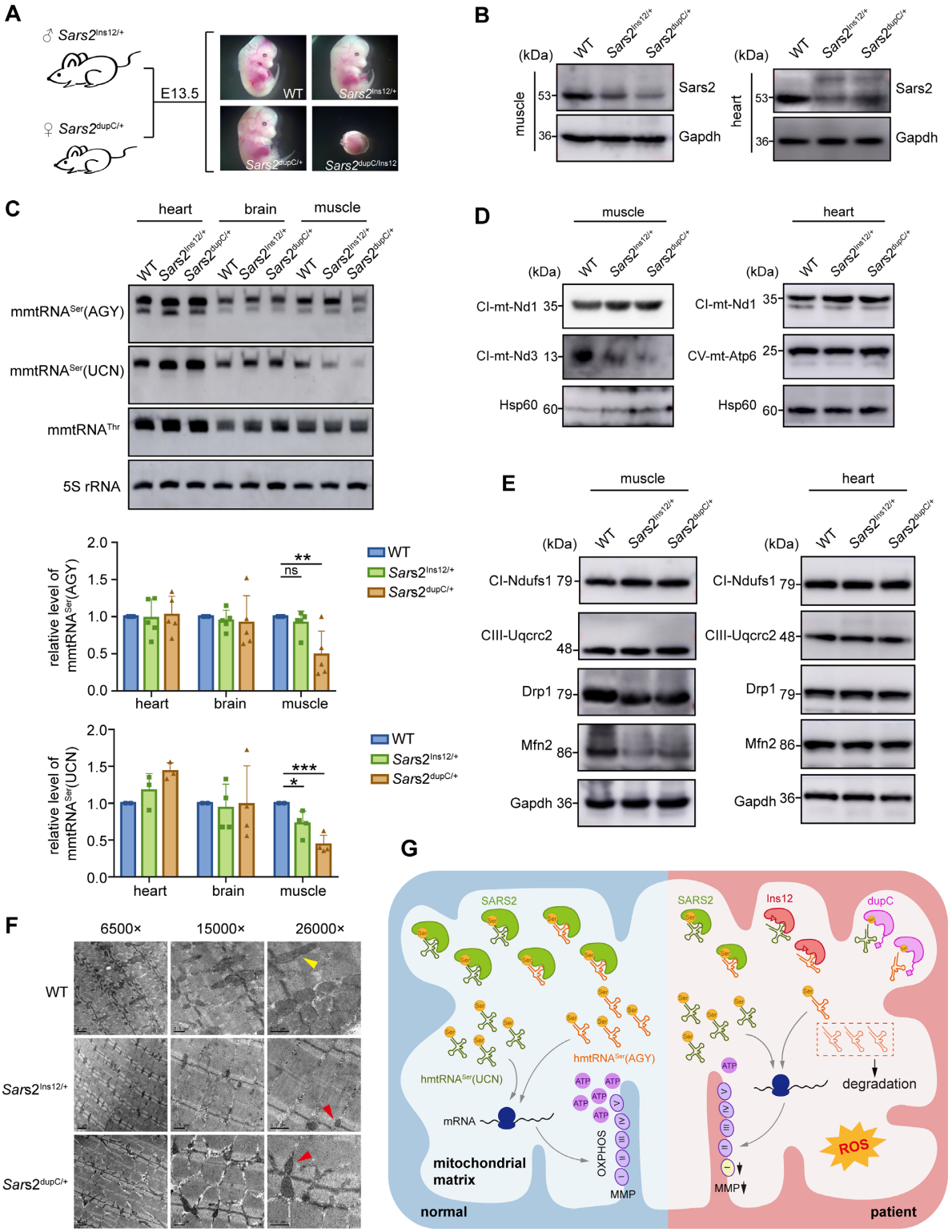

Figure 7. *Sars2* mutations caused embryonic lethality in mice and led to impaired mitochondrial translation and morphology in the skeletal muscle of heterozygous mice. (**A**) Mouse embryos at E13.5, showing fetal arrest in *Sars2*$^{Ins12/dupC}$ mice. (**B**) Steady-state levels of Sars2 in skeletal muscle and heart tissues. Gapdh was used as a loading control. (**C**) Steady-state abundance of mitochondrial tRNAs detected in heart, brain, and skeletal muscle tissues; 5S rRNA was used as the loading control. Data were normalized to those of the wild-type mice (lower panels). Values are expressed as mean ± SD ($n = 4$–5). *P* values were determined using the unpaired two-tailed t-test. $^{*}P < 0.05$, $^{**}P < 0.01$, $^{***}P < 0.001$; ns, not significant. (**D**) Western blot analysis of mtDNA-encoded proteins in the skeletal muscle and heart tissues. Hsp60 was used as a loading control. (**E**) Western blot analysis of nDNA-encoded proteins in the skeletal muscle and heart tissues. Gapdh was used as the loading control. (**F**) Mitochondria in skeletal muscle tissues were observed by TEM. Yellow arrowhead indicates morphologically normal mitochondria; red arrowheads indicate abnormal mitochondria. (**G**) Model of the molecular etiology underlying Ins12 and dupC-induced human disease.

Sars2$^{dupC/+}$ mice than those in wild-type mice, at one month of age. No obvious dupC was detected for Sars2$^{dupC/+}$ mice (Figure 7B). Sars2 levels in the brain tissue among wild-type, *Sars2*$^{Ins12/+}$ and *Sars2*$^{dupC/+}$ mice showed no obvious difference (Supplementary Figure S7C).

Northern blot showed that the steady-state levels of both mouse mitochondrial tRNA^{Ser}(AGY) (mmtRNA^{Ser}(AGY)) and mmtRNA^{Ser}(UCN) were comparable between the hearts and brains of various mice (Figure 7C). mmtRNA^{Ser}(AGY) level in skeletal muscle from *Sars2*$^{dupC/+}$ mice was 50% lower than that from wild-type mice, but remained unaltered in *Sars2*$^{Ins12/+}$ mice (Figure 7C). In addition, mmtRNA^{Ser}(UCN) levels in *Sars2*$^{Ins12/+}$ and *Sars2*$^{dupC/+}$ mice were significantly lower to 75% and 40%, respectively, when compared with that in wild-type mice (Figure 7C). These results suggest that the stability of mmtRNA^{Ser}(AGY) and mmtRNA^{Ser}(UCN) were highly sensitive to impairment of Sars2 function in skeletal muscle; however, despite noticeably lower levels of Sars2 in the heart, little influence on mmtRNA^{Ser}(AGY) and mmtRNA^{Ser}(UCN) was observed, suggesting tissue-specific dependence and vulnerability of mitochondrial tRNA^{Ser}s to Sars2. The charging levels of mmtRNA^{Ser}(AGY) and mmtRNA^{Ser}(UCN) in the heart, brain, and skeletal muscle were comparable between heterozygous and wild-type mice (Supplementary Figure S7D), which was consistent with the results in human iPSCs that (the remaining) mitochondrial tRNA^{Ser}s were nearly fully aminoacylated.

As seen in patient iPSCs, mt-Nd3 level in skeletal muscle from *Sars2*$^{dupC/+}$ and *Sars2*$^{Ins12/+}$ mice was obviously reduced compared with that in wild-type mice, whereas mt-Nd1 abundance was not affected (Figure 7D). However, no alteration in the expression of nDNA-encoded OXPHOS subunits, including Ndufs1 and Uqcrc2, was observed in the skeletal muscle (Figure 7D). In line with the lack of decrease in both tRNA^{Ser} abundance and tRNA charging levels, mitochondrial translation in the mouse heart was not affected, as evidenced by comparable levels of mtDNA-encoded mt-Nd1 and mt-Atp6 among groups (Figure 7D). No changes in Ndufs1 or Uqcrc2 expression were observed in mouse heart tissue (Figure 7E). Moreover, no abnormal protein levels were observed in the brains of heterozygous mice (Supplementary Figure S7C). These results suggest that the muscle tissue–specific downregulation of mitochondrial mRNA translation occurred in heterozygotes.

Western blot revealed that Drp1 and Mfn2 levels were lower in muscle tissue of *Sars2*$^{Ins12/+}$ (Drp1: 71.6%; Mfn2: 78.6% of wild-type) and *Sars2*$^{dupC/+}$ (Drp1: 92.5%; Mfn2: 77.9% of wild-type) mice, but not heart tissue of heterozygous mice (Figure 7E). Mitochondrial morphology in the mouse heart, brain, and skeletal muscle tissues was observed by TEM, which showed that the number and structure of mitochondria in the heart and brain tissues were not apparently different between heterozygous and wild-type mice (Supplementary Figure S7E). However, mitochondria in the skeletal muscle of heterozygous mice were fewer in number and smaller in size than those in wild-type mice (Figure 7F).

We further explored whether mitochondrial translation defects in the muscle yielded phenotypic consequences in male mice at 13–16 weeks of age. No obvious histological abnormalities were found in the rectus femoris muscle sections of *Sars2*$^{dupC/+}$ or *Sars2*$^{Ins12/+}$ mice. Quantification of the myofiber cross-sectional area also showed no significant difference in myofiber size distribution among wild-type and mutant mice (Supplementary Figure S7F). In the treadmill test, three groups of mice showed no significant difference in running time (Supplementary Figure S7G). No significant difference was observed between groups in the treadmill speed when mice were exhausted (Supplementary Figure S7G).

Altogether, the above evidence indicates that mmtRNA^{Ser}(UCN) and/or mmtRNA^{Ser}(AGY) levels were reduced in muscle from both *Sars2*$^{dupC/+}$ and *Sars2*$^{Ins12/+}$ mice, which subsequently led to impaired mitochondrial translation and morphology in heterozygotes.

DISCUSSION

SARS2 is highly associated with HUPRA syndrome and progressive spastic paresis (21–26). The clinical features of our patient overlapped with the phenotypes of both previously reported HUPRA syndrome and progressive spastic paresis (Supplementary Table S4). However, compared with HUPRA syndrome, the condition of the patient progressed more slowly, and the disease severity was relatively moderate. Metabolic alkalosis and premature birth, which are common in patients with HUPRA syndrome, were absent in this patient. The nervous system, which only affects progressive spastic paresis, was more seriously damaged in our patient. Hypertonia and varying degrees of paralysis observed in patients with *SARS2*-related progressive spastic paresis were also present in our patient. Moreover, frequent seizures, which have not been reported in *SARS2*-related patients, were one of the most striking features in our patient. Thus, our findings expanded the spectrum of the *SARS2*-related diseases.

The aminoacylation kinetics of Ins12 for both tRNA^{Ser}s could not be accurately quantified. Considering that Ins12 could activate Ser and bind tRNA^{Ser}s, its inability to aminoacylate tRNAs suggested that the enlarged loop B failed to orient the CCA terminus to synthetic active site. dupC exhibited a nearly 6-fold K_m value for hmtRNA^{Ser}(AGY) but that for hmtRNA^{Ser}(UCN) was only marginally increased. Moreover, The K_D determination echoed the aminoacylation kinetic data that the affinity of dupC for hmtRNA^{Ser}(AGY) was more significantly impaired. These data suggest a more critical role of the C-terminal tail for binding hmtRNA^{Ser}(AGY) in catalysis, in accordance with the previously reported results (19). Indeed, a very recent study has reported the cyro-EM structure of SARS2-tRNA^{Ser}(AGY), which clearly shows that the very C-terminus provides an important interaction site for binding the T-stem sugar-phosphate backbone of tRNA^{Ser}(AGY) (54).

The binding affinity and charging level of both mutants for hmtRNA^{Ser}(AGY) were dramatically impaired *in vitro*. Accordingly, *in vivo*, hmtRNA^{Ser}(AGY) abundance in patient cells was only 25% of that in control cells. Consistently, a reduced amount of hmtRNA^{Ser}(AGY) was also observed in HUPRA patients with a *SARS2*

c.1169A > G mutation, and in patients carrying the *SARS2* c.1347G > A mutation with progressive spastic paresis (21,25). We therefore suggest that *SARS2* mutations weakened the binding affinity for hmtRNA^{Ser}(AGY), leading to defects in the aminoacylation of hmtRNA^{Ser}(AGY) by both mutants. Subsequently, impaired aminoacylation of hmtRNA^{Ser}(AGY) led to the naked hmtRNA^{Ser}(AGY), which is more prone to degradation by the mitochondrial RNA degradosome (55,56) and thus could not be detected by northern blot analysis. However, the residual aminoacylated hmtRNA^{Ser}(AGY) remained intact; therefore, we visualized seemingly unchanged aminoacylation levels of hmtRNA^{Ser}(AGY) when compared with maternal, paternal, and control cell lines, suggesting hmtRNA^{Ser}(AGY) integrity was protected from degradation by tRNA aminoacylation. Besides, we cannot absolutely exclude the possibility that SARS2 was able to serve as a tRNA 'chaperone' to stabilize, in particular, the unusual tRNA^{Ser}(AGY). With a reduced abundance of SARS2 and its mutants in patient cells, tRNA^{Ser}(AGY) was more prone to be degraded. Such a chaperone role has been observed for LARS2 and its C-terminal domain (57,58). The residual pool of Ser-hmtRNA^{Ser}(AGY) subsequently caused an abnormal rate of mitochondrial translation. Common observations of reduced hmtRNA^{Ser}(AGY) in different patients (21,25), albeit with distinct clinical manifestations, suggest that a decreased level of hmtRNA^{Ser}(AGY) due to rapid degradation of uncharged hmtRNA^{Ser}(AGY) is the primary etiology of *SARS2*-related diseases reported to date.

Several studies with other mitochondrial aaRS-related diseases have also described similar downregulation of cognate tRNA levels. The level of mitochondrial tRNA^{Asn} was markedly reduced while its aminoacylation level seems to be unaltered in a patient with *NARS2* mutations (59). An intronic mutation in *RARS2* causes a truncated ArgRS and a lower amount of mitochondrial tRNA^{Arg}, while the remaining transcript is fully aminoacylated (60). In addition, the steady-state level of mitochondrial tRNA^{Tyr} is reduced in the cell lines derived from patients with Leber's hereditary optic neuropathy (LHON) phenotypes due to a *YARS2* c.572G > T mutation (61). All these examples suggested that aminoacylation status of some mitochondrial tRNAs determines its cellular abundance. In line with this suggestion, we found that re-expression of wild-type *SARS2* was able to restore hmtRNA^{Ser}(AGY) amount to a comparable level with control cell lines. In addition, the restored hmtRNA^{Ser}(AGY) was fully charged. Consistently, overexpression of *LARS2* could improve the aminoacylation efficiency and stability of mitochondrial tRNA^{Leu}(UUR) A3243G mutant, which leads to tRNA^{Leu}(UUR) instability and Mitochondrial Encephalopathy, Lactic Acidosis, and Stroke-like episodes (MELAS) syndrome (62); likewise, *HARS2* overexpression in cybrids carrying the m. 12201 T > C mutation elevates the steady-state level of the mitochondrial tRNA^{His} mutant (63).

Previous studies have uncovered that aberrant mitochondrial tRNA species are prone to be spuriously polyadenylated following the 3-terminal A76 by mitochondrial poly(A)polymerase (mtPAP) (64) and subsequently degraded by the mitochondrial degradosome, composed of polynucleotide phosphorylase (PNPase) and the RNA helicase SUV3 (56). On other hand, 2′,5′-phosphodiesterase PDE12 functions as an important tRNA surveillance factor to remove such spurious poly(A) tails (64,65). The balance of polyadenylation and de-adenylation likely provides a strategy to regulate tRNA abundance and to retain a functional tRNA pool in human mitochondria. Of note, in most cases, the poly(A) modification and degradation occur at the structurally aberrant tRNAs (7,56,64,65). Here, we suggested that naked A76 of hmtRNA^{Ser}(AGY) is easily polyadenylated by mtPAP despite that hmtRNA^{Ser}(AGY) is native without structural variation and the competition of de-adenylation by PDE12 likely insufficiently compromised the destructive effect on hmtRNA^{Ser}(AGY) stability. Considering decreased level of hmtRNA^{Ser}(AGY) seems to underlie all *SARS2*-related human mitochondrial disease, the hmtRNA^{Ser}(AGY) metabolism needs to be further explored. Elevating abundance of hmtRNA^{Ser}(AGY) based on its metabolism pathway might provide therapeutic potential for treatment of *SARS2*-related diseases. Beside overexpression of *SARS2* explored here, manipulation of processes in hmtRNA^{Ser}(AGY) lifecycle, including t^6A modification by YRDC-OSGEPL1 (32,66), m^3C biogenesis by NSUN2 (67,68), poly(A) addition by mtPAP (64), de-adenylation by PDE12 (65), degradation by degradosome (56) etc, if elevating its abundance, poses promising potentials to improve *SARS2*-related mitochondrial diseases. In addition, mitochondria from both lower and higher eukaryotes are able to import nuclear-expressed tRNAs (69,70). It is worthy to explore any possibility to overexpress and import nuclear-expressed hmtRNA^{Ser}(AGY) to increase its organelle concentration as a treatment choice for *SARS2*-related mitochondrial diseases.

The mechanisms of tissue-specific involvement in mito-aaRS-related diseases remain unclear at present (71). Various sensitivities of mitochondrial tRNA^{Ser}s to SARS2 in different organs may contribute to its tissue specificity, albeit why tRNA^{Ser}s are selectively decreased in muscle tissue is still unclear.

In summary, we identified two novel *SARS2* variants in a Chinese pedigree. These two mutations led to reduced SARS2 abundance and remodeling of the SARS2 local structure. The weakened tRNA binding capacity, which was particularly pronounced for tRNA^{Ser}(AGY), caused impaired or abolished tRNA^{Ser}(AGY) aminoacylation, which subsequently resulted in its rapid degradation and thus insufficient aminoacylation of tRNA^{Ser}(AGY) in patient cells, leading to pleiotropic defects in mitochondrial biogenesis, homeostasis, and function (Figure 7G). The destructive effect of either mutation on tRNA^{Ser}(AGY) stability, mitochondrial function, and animal viability was also observed in mouse models. Our findings expand the *SARS2*-related disease spectrum and clarify the molecular etiology of *SARS2* mutations.

DATA AVAILABILITY

Structures of WT SARS2 and Ins12 have been deposited to PDB database with accession codes 7YDF and 7YDG. All other data supporting the findings of this study are available within the article and its Supplementary Information.

SUPPLEMENTARY DATA

Supplementary Data are available at NAR Online.

ACKNOWLEDGEMENTS

We are grateful to Prof. En-Duo Wang (Shanghai Institute of Biochemistry and Cell Biology, CAS) for consistent support and encouragement. We thank Prof. Yanxin Li (Shanghai Children's Medical Center) for the assistance in iPSCs generation.

Author contributions: X.Z. conceptualized, designed and coordinated the study, performed *in vitro* biochemical studies and drafted and revised the manuscript. J.W. conceptualized and coordinated the study, and revised the manuscript. T.Y. and Y.Z. carried out most of the experiments, and drafted and revised the manuscript. W.Z., Y.Z. and G.L. contributed to several experiments and helped with data analysis. J.W., R.Y. and N.L. performed the genetic tests, interpreted the variations and evaluated the phenotype. W.S. and P.F. performed protein structure analysis.

FUNDING

National Key Research and Development Program of China [2021YFA1300800, 2021YFC2700903 to X.Z. and 2020YFA0804000 to J.W.]; Natural Science Foundation of China [82171849 to T.Y. and 31822015, 81870896, 32271300 to X.Z.]; Committee of Science and Technology in Shanghai [22ZR1481300, 22JC1400503 to X.Z.]; CAS Project for Young Scientists in Basic Research [YSBR-075 to X.Z.]; State Key Laboratory of Bioorganic and Natural Products Chemistry (to P.F.). Funding for open access charge: the National Key Research and Development Program of China.

Conflict of interest statement. None declared.

REFERENCES

1. Chen,Y., Liu,Y. and Dorn,G.W. 2nd (2011) Mitochondrial fusion is essential for organelle function and cardiac homeostasis. *Circ. Res.*, **109**, 1327–1331.
2. Ikeda,Y., Shirakabe,A., Maejima,Y., Zhai,P., Sciarretta,S., Toli,J., Nomura,M., Mihara,K., Egashira,K., Ohishi,M. *et al.* (2015) Endogenous drp1 mediates mitochondrial autophagy and protects the heart against energy stress. *Circ. Res.*, **116**, 264–278.
3. Simon,H.U., Haj-Yehia,A. and Levi-Schaffer,F. (2000) Role of reactive oxygen species (ROS) in apoptosis induction. *Apoptosis*, **5**, 415–418.
4. Koyano,F., Okatsu,K., Kosako,H., Tamura,Y., Go,E., Kimura,M., Kimura,Y., Tsuchiya,H., Yoshihara,H., Hirokawa,T. *et al.* (2014) Ubiquitin is phosphorylated by PINK1 to activate parkin. *Nature*, **510**, 162–166.
5. Murakawa,T., Yamaguchi,O., Hashimoto,A., Hikoso,S., Takeda,T., Oka,T., Yasui,H., Ueda,H., Akazawa,Y., Nakayama,H. *et al.* (2015) Bcl-2-like protein 13 is a mammalian atg32 homologue that mediates mitophagy and mitochondrial fragmentation. *Nat. Commun.*, **6**, 7527.
6. Suzuki,T., Nagao,A. and Suzuki,T. (2011) Human mitochondrial tRNAs: biogenesis, function, structural aspects, and diseases. *Annu. Rev. Genet.*, **45**, 299–329.
7. Kummer,E. and Ban,N. (2021) Mechanisms and regulation of protein synthesis in mitochondria. *Nat. Rev. Mol. Cell Biol.*, **22**, 307–325.
8. Hallberg,B.M. and Larsson,N.G. (2014) Making proteins in the powerhouse. *Cell Metab.*, **20**, 226–240.
9. Eriani,G., Delarue,M., Poch,O., Gangloff,J. and Moras,D. (1990) Partition of tRNA synthetases into two classes based on mutually exclusive sets of sequence motifs. *Nature*, **347**, 203–206.
10. Ibba,M. and Soll,D. (2000) Aminoacyl-tRNA synthesis. *Annu. Rev. Biochem.*, **69**, 617–650.
11. Guo,M., Yang,X.L. and Schimmel,P. (2010) New functions of aminoacyl-tRNA synthetases beyond translation. *Nat. Rev. Mol. Cell Biol.*, **11**, 668–674.
12. Antonellis,A. and Green,E.D. (2008) The role of aminoacyl-tRNA synthetases in genetic diseases. *Annu. Rev. Genomics Hum. Genet.*, **9**, 87–107.
13. Bonnefond,L., Fender,A., Rudinger-Thirion,J., Giege,R., Florentz,C. and Sissler,M. (2005) Toward the full set of human mitochondrial aminoacyl-tRNA synthetases: characterization of AspRS and TyrRS. *Biochemistry*, **44**, 4805–4816.
14. Moulinier,L., Ripp,R., Castillo,G., Poch,O. and Sissler,M. (2017) MiSynPat: an integrated knowledge base linking clinical, genetic, and structural data for disease-causing mutations in human mitochondrial aminoacyl-tRNA synthetases. *Hum. Mutat.*, **38**, 1316–1324.
15. Sissler,M., Gonzalez-Serrano,L.E. and Westhof,E. (2017) Recent advances in mitochondrial aminoacyl-tRNA synthetases and disease. *Trends Mol. Med.*, **23**, 693–708.
16. Yao,P. and Fox,P.L. (2013) Aminoacyl-tRNA synthetases in medicine and disease. *EMBO Mol. Med.*, **5**, 332–343.
17. Lightowlers,R.N., Taylor,R.W. and Turnbull,D.M. (2015) Mutations causing mitochondrial disease: what is new and what challenges remain? *Science*, **349**, 1494–1499.
18. Yokogawa,T., Shimada,N., Takeuchi,N., Benkowski,L., Suzuki,T., Omori,A., Ueda,T., Nishikawa,K., Spremulli,L.L. and Watanabe,K. (2000) Characterization and tRNA recognition of mammalian mitochondrial seryl-tRNA synthetase. *J. Biol. Chem.*, **275**, 19913–19920.
19. Chimnaronk,S., Gravers Jeppesen,M., Suzuki,T., Nyborg,J. and Watanabe,K. (2005) Dual-mode recognition of noncanonical tRNAs(Ser) by seryl-tRNA synthetase in mammalian mitochondria. *EMBO J.*, **24**, 3369–3379.
20. Chan,P.P. and Lowe,T.M. (2016) GtRNAdb 2.0: an expanded database of transfer RNA genes identified in complete and draft genomes. *Nucleic Acids Res.*, **44**, D184–D189.
21. Belostotsky,R., Ben-Shalom,E., Rinat,C., Becker-Cohen,R., Feinstein,S., Zeligson,S., Segel,R., Elpeleg,O., Nassar,S. and Frishberg,Y. (2011) Mutations in the mitochondrial seryl-tRNA synthetase cause hyperuricemia, pulmonary hypertension, renal failure in infancy and alkalosis, HUPRA syndrome. *Am. J. Hum. Genet.*, **88**, 193–200.
22. Rivera,H., Martin-Hernandez,E., Delmiro,A., Garcia-Silva,M.T., Quijada-Fraile,P., Muley,R., Arenas,J., Martin,M.A. and Martinez-Azorin,F. (2013) A new mutation in the gene encoding mitochondrial seryl-tRNA synthetase as a cause of HUPRA syndrome. *BMC Nephrol.*, **14**, 195.
23. Zhou,Y., Zhong,C., Yang,Q., Zhang,G., Yang,H., Li,Q. and Wang,M. (2021) Novel *SARS2* variants identified in a chinese girl with HUPRA syndrome. *Mol. Genet. Genomic Med.*, **9**, e1650.
24. Colin,E., Courtois,G., Brouzes,C., Pulman,J., Rabant,M., Rotig,A., Taffin,H., Lion-Lambert,M., Fabrega,S., Da Costa,L. *et al.* (2021) Biallelic mutations in the *SARS2* gene presenting as congenital sideroblastic anemia. *Haematologica*, **106**, 3202–3205.
25. Linnankivi,T., Neupane,N., Richter,U., Isohanni,P. and Tyynismaa,H. (2016) Splicing defect in mitochondrial seryl-tRNA synthetase gene causes progressive spastic paresis instead of HUPRA syndrome. *Hum. Mutat.*, **37**, 884–888.
26. Souza,P.V.S., Bortholin,T., Dias,R.B., Chieia,M.A.T., Burlin,S., Naylor,F.G.M., Pinto,W. and Oliveira,A.S.B. (2017) New genetic causes for complex hereditary spastic paraplegia. *J. Neurol. Sci.*, **379**, 283–292.
27. Dahary,D., Golan,Y., Mazor,Y., Zelig,O., Barshir,R., Twik,M., Iny Stein,T., Rosner,G., Kariv,R., Chen,F. *et al.* (2019) Genome analysis and knowledge-driven variant interpretation with TGex. *BMC Med. Genomics*, **12**, 200.
28. Gu,H., Huang,X., Xu,J., Song,L., Liu,S., Zhang,X.B., Yuan,W. and Li,Y. (2018) Optimizing the method for generation of integration-free induced pluripotent stem cells from human peripheral blood. *Stem Cell Res. Ther.*, **9**, 163.
29. Fernandez-Vizarra,E., Ferrin,G., Perez-Martos,A., Fernandez-Silva,P., Zeviani,M. and Enriquez,J.A. (2010) Isolation of mitochondria for biogenetical studies: an update. *Mitochondrion*, **10**, 253–262.

30. Sasarman,F., Antonicka,H. and Shoubridge,E.A. (2008) The A3243G $tRNA^{Leu}$(UUR) MELAS mutation causes amino acid misincorporation and a combined respiratory chain assembly defect partially suppressed by overexpression of EFTu and EFG2. *Hum. Mol. Genet.*, **17**, 3697–3707.
31. Mao,X.L., Li,Z.H., Huang,M.H., Wang,J.T., Zhou,J.B., Li,Q.R., Xu,H., Wang,X.J. and Zhou,X.L. (2021) Mutually exclusive substrate selection strategy by human m^3C RNA transferases METTL2A and METTL6. *Nucleic Acids Res.*, **49**, 8309–8323.
32. Zhou,J.B., Wang,Y., Zeng,Q.Y., Meng,S.X., Wang,E.D. and Zhou,X.L. (2020) Molecular basis for t^6A modification in human mitochondria. *Nucleic Acids Res.*, **48**, 3181–3194.
33. Huang,M.H., Peng,G.X., Mao,X.L., Wang,J.T., Zhou,J.B., Zhang,J.H., Chen,M., Wang,E.D. and Zhou,X.L. (2022) Molecular basis for human mitochondrial tRNA m^3C modification by alternatively spliced METTL8. *Nucleic Acids Res.*, **50**, 4012–4028.
34. Zhou,X.L., Zhu,B. and Wang,E.D. (2008) The CP2 domain of leucyl-tRNA synthetase is crucial for amino acid activation and post-transfer editing. *J. Biol. Chem.*, **283**, 36608–36616.
35. Otwinowski,Z. and Minor,W. (1997) Processing of X-ray diffraction data collected in oscillation mode. *Methods Enzymol.*, **276**, 307–326.
36. Vagin,A. and Teplyakov,A. (2010) Molecular replacement with MOLREP. *Acta Crystallogr. D Biol. Crystallogr.*, **66**, 22–25.
37. Emsley,P., Lohkamp,B., Scott,W.G. and Cowtan,K. (2010) Features and development of coot. *Acta Crystallogr. D Biol. Crystallogr.*, **66**, 486–501.
38. Adams,P.D., Afonine,P.V., Bunkoczi,G., Chen,V.B., Davis,I.W., Echols,N., Headd,J.J., Hung,L.W., Kapral,G.J., Grosse-Kunstleve,R.W. *et al.* (2010) PHENIX: a comprehensive Python-based system for macromolecular structure solution. *Acta Crystallogr. D Biol. Crystallogr.*, **66**, 213–221.
39. Biou,V., Yaremchuk,A., Tukalo,M. and Cusack,S. (1994) The 2.9 a crystal structure of *t. thermophilus* seryl-tRNA synthetase complexed with tRNA(Ser). *Science*, **263**, 1404–1410.
40. Jumper,J., Evans,R., Pritzel,A., Green,T., Figurnov,M., Ronneberger,O., Tunyasuvunakool,K., Bates,R., Zidek,A., Potapenko,A. *et al.* (2021) Highly accurate protein structure prediction with alphafold. *Nature*, **596**, 583–589.
41. Varadi,M., Anyango,S., Deshpande,M., Nair,S., Natassia,C., Yordanova,G., Yuan,D., Stroe,O., Wood,G., Laydon,A. *et al.* (2022) AlphaFold protein structure database: massively expanding the structural coverage of protein-sequence space with high-accuracy models. *Nucleic Acids Res.*, **50**, D439–D444.
42. Blocquel,D., Li,S., Wei,N., Daub,H., Sajish,M., Erfurth,M.L., Kooi,G., Zhou,J., Bai,G., Schimmel,P. *et al.* (2017) Alternative stable conformation capable of protein misinteraction links tRNA synthetase to peripheral neuropathy. *Nucleic Acids Res.*, **45**, 8091–8104.
43. Fukuhara,H. and Kujawa,C. (1970) Selective inhibition of the *in vivo* transcription of mitochondrial DNA by ethidium bromide and by acriflavin. *Biochem. Biophys. Res. Commun.*, **41**, 1002–1008.
44. Hayakawa,T., Noda,M., Yasuda,K., Yorifuji,H., Taniguchi,S., Miwa,I., Sakura,H., Terauchi,Y., Hayashi,J., Sharp,G.W. *et al.* (1998) Ethidium bromide-induced inhibition of mitochondrial gene transcription suppresses glucose-stimulated insulin release in the mouse pancreatic beta-cell line betaHC9. *J. Biol. Chem.*, **273**, 20300–20307.
45. Gustafsson,C.M., Falkenberg,M. and Larsson,N.G. (2016) Maintenance and expression of mammalian mitochondrial DNA. *Annu. Rev. Biochem.*, **85**, 133–160.
46. Wiedemann,N. and Pfanner,N. (2017) Mitochondrial machineries for protein import and assembly. *Annu. Rev. Biochem.*, **86**, 685–714.
47. Vercellino,I. and Sazanov,L.A. (2022) The assembly, regulation and function of the mitochondrial respiratory chain. *Nat. Rev. Mol. Cell Biol.*, **23**, 141–161.
48. Zorova,L.D., Popkov,V.A., Plotnikov,E.Y., Silachev,D.N., Pevzner,I.B., Jankauskas,S.S., Babenko,V.A., Zorov,S.D., Balakireva,A.V., Juhaszova,M. *et al.* (2018) Mitochondrial membrane potential. *Anal. Biochem.*, **552**, 50–59.
49. Palma,F.R., He,C., Danes,J.M., Paviani,V., Coelho,D.R., Gantner,B.N. and Bonini,M.G. (2020) Mitochondrial superoxide dismutase: what the established, the intriguing, and the novel reveal about a key cellular redox switch. *Antioxid. Redox Signal.*, **32**, 701–714.
50. Tretter,L. and Adam-Vizi,V. (2004) Generation of reactive oxygen species in the reaction catalyzed by alpha-ketoglutarate dehydrogenase. *J. Neurosci.*, **24**, 7771–7778.
51. Cattaruzza,M. and Hecker,M. (2008) Protein carbonylation and decarboylation: a new twist to the complex response of vascular cells to oxidative stress. *Circ. Res.*, **102**, 273–274.
52. Sciarretta,S., Maejima,Y., Zablocki,D. and Sadoshima,J. (2018) The role of autophagy in the heart. *Annu. Rev. Physiol.*, **80**, 1–26.
53. Mauvezin,C. and Neufeld,T.P. (2015) Bafilomycin A1 disrupts autophagic flux by inhibiting both V-ATPase-dependent acidification and Ca-P60A/SERCA-dependent autophagosome-lysosome fusion. *Autophagy*, **11**, 1437–1438.
54. Kuhle,B., Hirschi,M., Doerfel,L.K., Lander,G.C. and Schimmel,P. (2022) Structural basis for shape-selective recognition and aminoacylation of a D-armless human mitochondrial tRNA. *Nat. Commun.*, **13**, 5100.
55. Borowski,L.S., Dziembowski,A., Hejnowicz,M.S., Stepien,P.P. and Szczesny,R.J. (2013) Human mitochondrial RNA decay mediated by PNPase-hSuv3 complex takes place in distinct foci. *Nucleic Acids Res.*, **41**, 1223–1240.
56. Toompuu,M., Tuomela,T., Laine,P., Paulin,L., Dufour,E. and Jacobs,H.T. (2018) Polyadenylation and degradation of structurally abnormal mitochondrial tRNAs in human cells. *Nucleic Acids Res.*, **46**, 5209–5226.
57. Perli,E., Giordano,C., Pisano,A., Montanari,A., Campese,A.F., Reyes,A., Ghezzi,D., Nasca,A., Tuppen,H.A., Orlandi,M. *et al.* (2014) The isolated carboxy-terminal domain of human mitochondrial leucyl-tRNA synthetase rescues the pathological phenotype of mitochondrial tRNA mutations in human cells. *EMBO Mol. Med.*, **6**, 169–182.
58. Hornig-Do,H.T., Montanari,A., Rozanska,A., Tuppen,H.A., Almalki,A.A., Abg-Kamaludin,D.P., Frontali,L., Francisci,S., Lightowlers,R.N. and Chrzanowska-Lightowlers,Z.M. (2014) Human mitochondrial leucyl tRNA synthetase can suppress non cognate pathogenic mt-tRNA mutations. *EMBO Mol. Med.*, **6**, 183–193.
59. Simon,M., Richard,E.M., Wang,X., Shahzad,M., Huang,V.H., Qaiser,T.A., Potluri,P., Mahl,S.E., Davila,A., Nazli,S. *et al.* (2015) Mutations of human *NARS2*, encoding the mitochondrial asparaginyl-tRNA synthetase, cause nonsyndromic deafness and leigh syndrome. *PLos Genet.*, **11**, e1005097.
60. Edvardson,S., Shaag,A., Kolesnikova,O., Gomori,J.M., Tarassov,I., Einbinder,T., Saada,A. and Elpeleg,O. (2007) Deleterious mutation in the mitochondrial arginyl-transfer RNA synthetase gene is associated with pontocerebellar hypoplasia. *Am. J. Hum. Genet.*, **81**, 857–862.
61. Riley,L.G., Cooper,S., Hickey,P., Rudinger-Thirion,J., McKenzie,M., Compton,A., Lim,S.C., Thorburn,D., Ryan,M.T., Giege,R. *et al.* (2010) Mutation of the mitochondrial tyrosyl-tRNA synthetase gene, *YARS2*, causes myopathy, lactic acidosis, and sideroblastic anemia–MLASA syndrome. *Am. J. Hum. Genet.*, **87**, 52–59.
62. Li,R. and Guan,M.X. (2010) Human mitochondrial leucyl-tRNA synthetase corrects mitochondrial dysfunctions due to the $tRNA^{Leu}$(UUR) A3243G mutation, associated with mitochondrial encephalomyopathy, lactic acidosis, and stroke-like symptoms and diabetes. *Mol. Cell Biol.*, **30**, 2147–2154.
63. Gong,S., Wang,X., Meng,F., Cui,L., Yi,Q., Zhao,Q., Cang,X., Cai,Z., Mo,J.Q., Liang,Y. *et al.* (2020) Overexpression of mitochondrial histidyl-tRNA synthetase restores mitochondrial dysfunction caused by a deafness-associated tRNA(His) mutation. *J. Biol. Chem.*, **295**, 940–954.
64. Fiedler,M., Rossmanith,W., Wahle,E. and Rammelt,C. (2015) Mitochondrial poly(A) polymerase is involved in tRNA repair. *Nucleic Acids Res.*, **43**, 9937–9949.
65. Pearce,S.F., Rorbach,J., Van Haute,L., D'Souza,A.R., Rebelo-Guiomar,P., Powell,C.A., Brierley,I., Firth,A.E. and Minczuk,M. (2017) Maturation of selected human mitochondrial tRNAs requires deadenylation. *Elife*, **6**, e27596.
66. Lin,H., Miyauchi,K., Harada,T., Okita,R., Takeshita,E., Komaki,H., Fujioka,K., Yagasaki,H., Goto,Y.I., Yanaka,K. *et al.* (2018) co_2-sensitive tRNA modification associated with human mitochondrial disease. *Nat. Commun.*, **9**, 1875.
67. Shinoda,S., Kitagawa,S., Nakagawa,S., Wei,F.Y., Tomizawa,K., Araki,K., Araki,M., Suzuki,T. and Suzuki,T. (2019) Mammalian

NSUN2 introduces 5-methylcytidines into mitochondrial tRNAs. *Nucleic Acids Res.*, **47**, 8734–8745.
68. Van Haute,L., Lee,S.Y., McCann,B.J., Powell,C.A., Bansal,D., Vasiliauskaite,L., Garone,C., Shin,S., Kim,J.S., Frye,M. *et al.* (2019) NSUN2 introduces 5-methylcytosines in mammalian mitochondrial tRNAs. *Nucleic Acids Res.*, **47**, 8720–8733.
69. Duchene,A.M., Pujol,C. and Marechal-Drouard,L. (2009) Import of tRNAs and aminoacyl-tRNA synthetases into mitochondria. *Curr. Genet.*, **55**, 1–18.
70. Mercer,T.R., Neph,S., Dinger,M.E., Crawford,J., Smith,M.A., Shearwood,A.M., Haugen,E., Bracken,C.P., Rackham,O., Stamatoyannopoulos,J.A. *et al.* (2011) The human mitochondrial transcriptome. *Cell*, **146**, 645–658.
71. Gonzalez-Serrano,L.E., Chihade,J.W. and Sissler,M. (2019) When a common biological role does not imply common disease outcomes: disparate pathology linked to human mitochondrial aminoacyl-tRNA synthetases. *J. Biol. Chem.*, **294**, 5309–5320.